Parental histone transfer caught at the replication fork

https://doi.org/10.1038/s41586-024-07152-2

Received: 5 October 2023

Accepted: 1 February 2024

Published online: 6 March 2024

Check for updates

Ningning Li[1,9], Yuan Gao[2,9], Yujie Zhang[3,9], Daqi Yu[4,5,9], Jianwei Lin[5], Jianxun Feng[3], Jian Li[2], Zhichun Xu[2], Yingyi Zhang[6], Shangyu Dang[4], Keda Zhou[7], Yang Liu[7], Xiang David Li[5], Bik Kwoon Tye[8]✉, Qing Li[3]✉, Ning Gao[1]✉ & Yuanliang Zhai[2]✉

In eukaryotes, DNA compacts into chromatin through nucleosomes[1,2]. Replication of the eukaryotic genome must be coupled to the transmission of the epigenome encoded in the chromatin[3,4]. Here we report cryo-electron microscopy structures of yeast (*Saccharomyces cerevisiae*) replisomes associated with the FACT (facilitates chromatin transactions) complex (comprising Spt16 and Pob3) and an evicted histone hexamer. In these structures, FACT is positioned at the front end of the replisome by engaging with the parental DNA duplex to capture the histones through the middle domain and the acidic carboxyl-terminal domain of Spt16. The H2A–H2B dimer chaperoned by the carboxyl-terminal domain of Spt16 is stably tethered to the H3–H4 tetramer, while the vacant H2A–H2B site is occupied by the histone-binding domain of Mcm2. The Mcm2 histone-binding domain wraps around the DNA-binding surface of one H3–H4 dimer and extends across the tetramerization interface of the H3–H4 tetramer to the binding site of Spt16 middle domain before becoming disordered. This arrangement leaves the remaining DNA-binding surface of the other H3–H4 dimer exposed to additional interactions for further processing. The Mcm2 histone-binding domain and its downstream linker region are nested on top of Tof1, relocating the parental histones to the replisome front for transfer to the newly synthesized lagging-strand DNA. Our findings offer crucial structural insights into the mechanism of replication-coupled histone recycling for maintaining epigenetic inheritance.

In eukaryotes, chromosomal DNA is organized into chromatin with the nucleosome as the basic repeating unit comprising around 147 bp of duplex DNA, wrapped around two H2A–H2B dimers and one H3–H4 tetramer[1,2]. Post-translational modifications of histones further define diverse functional states of chromatin, which are transmittable to progenies[3,4]. During DNA replication, parental nucleosomes bearing epigenetic marks are disassembled ahead of each replication fork to enable duplex DNA unwinding and subsequent DNA synthesis[4–6]. To maintain the fidelity of the epigenetic landscape, the evicted parental histones are subsequently recycled to newly synthesized strands by well-recognized yet poorly understood replication-coupled mechanisms[4,5,7].

The machine dedicated to DNA replication, the replisome, is made up of at least three engines at its core: a CMG (Cdc45–Mcm2-7–GINS) helicase and two DNA polymerases, one on each strand[8–11]. Furthermore, multiple accessory factors, including the histone chaperone FACT, Ctf4, DNA polymerase α (Polα) and the fork protection complex comprising Tof1–Csm3 and Mrc1, are required to drive a fast and accurate replication through the nucleosome template[12–14]. FACT, which consists of Spt16 and Pob3 (homologue of SSRP1 in mammals)[15], has been implicated in replication fork passage through the nucleosome[13,16]. FACT recognizes and binds to partially unravelled nucleosomes to promote nucleosome disassembly by displacing H2A–H2B[17–19]. While translocating along the leading strand for DNA unwinding, the CMG helicase uses the N-terminal tier of its MCM ring as the front end[20,21], facing the parental nucleosomes. Some accessory factors including Ctf4, Polα, Tof1–Csm3 and Mrc1 are also placed at the same front[22–26]. Together, these factors are arranged in a strategic position to modulate nucleosome disassembly as well as parental histone recycling. Indeed, several replisome components exhibit histone chaperone activities. For example, a conserved histone-binding domain (HBD) from the N-terminal extension (NTE) (residues 1–200) of Mcm2 can wrap around the H3–H4 dimer to hijack its DNA-binding surface[27,28]. Pol1, the catalytic subunit of Polα, also contains a histone-binding motif[29,30]. Mutations in these components that disrupt their histone-binding abilities lead to defects in histone recycling to lagging strands[31,32]. Furthermore, Dpb3 (homologue of POLE4 in mammals) and Dpb4 (homologue of POLE3 in mammals), two subunits of leading strand DNA polymerase ε (Polε),

[1]State Key Laboratory of Membrane Biology, Peking-Tsinghua Center for Life Sciences, School of Life Sciences, Peking University, Beijing, China. [2]School of Biological Sciences, The University of Hong Kong, Hong Kong, China. [3]State Key Laboratory of Protein and Plant Gene Research, School of Life Sciences and Peking-Tsinghua Center for Life Sciences, Peking University, Beijing, China. [4]Division of Life Science, The Hong Kong University of Science & Technology, Hong Kong, China. [5]Department of Chemistry, The University of Hong Kong, Hong Kong, China. [6]Biological Cryo-EM Center, The Hong Kong University of Science and Technology, Hong Kong, China. [7]School of Biomedical Sciences, The University of Hong Kong, Hong Kong, China. [8]Department of Molecular Biology & Genetics, Cornell University, Ithaca, NY, USA. [9]These authors contributed equally: Ningning Li, Yuan Gao, Yujie Zhang, Daqi Yu. ✉e-mail: bt16@cornell.edu; li.qing@pku.edu.cn; gaon@pku.edu.cn; zhai@hku.hk

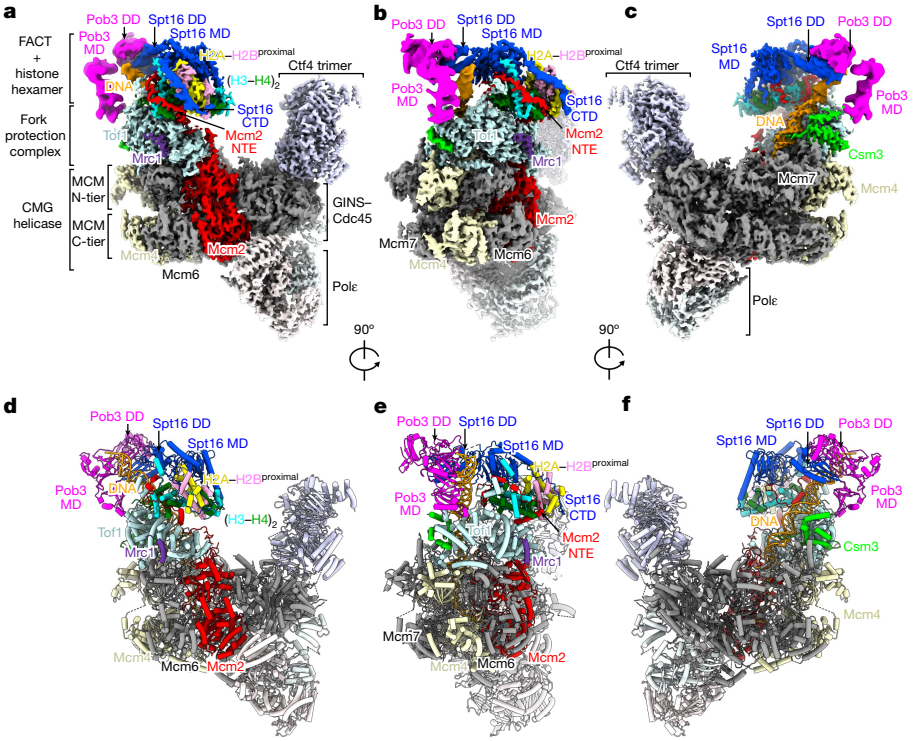

Fig. 1 | The overall structure of an endogenous replisome. a–c, Cryo-EM map of the replisome in complex with a stable FACT–histone shown in three representative views. The different parts of the map were combined with local optimization (Methods). **d–f**, The same as in **a–c**, respectively, but shown with the cylindrical atomic model. The MCM subunits, Ctf4, Tof1, Csm3, Mrc1, Spt16, Pob3 and histones are colour-coded and labelled as indicated.

have been implicated in the transfer of parental histones to leading strands[30,33]. A recent study also found that parental H2A–H2B can be recycled symmetrically using a mechanism distinct from the H3–H4 tetramer[34]. Despite these advances, questions remain unanswered regarding the molecular details of parental histone displacement, chaperoning and reassembly onto newly synthesized DNA strands, as well as the exact roles of FACT with various replisome components during these processes. One major reason can be attributed to the lack of high-resolution structures that catch the replisome in the act of shuffling parental histone transfer.

Characterization of native replisomes

To capture snapshots of parental histone transfer at the replication fork in vivo, we purified endogenous replisome complexes from early-S-phase yeast cells (*Psf2-3×Flag*) for structural characterization using cryo-electron microscopy (cryo-EM; Methods and Extended Data Fig. 1a–c). The isolated replisomes were first analysed using quantitative mass spectrometry (MS), showing high enrichment of CMG, histones, Ctf4, Tof1–Csm3, FACT, Mrc1 and Polε. By contrast, the levels of Polα and other associating factors were relatively low (Extended Data Fig. 1d and Supplementary Table 1), suggesting that their binding to the replisome core is weak or transient. Importantly, the replisomes exclusively carried parental histones as evidenced by the detection of the trimethylation at Lys4 of H3 (H3K4me3), a marker of parental histones, but not the acetylation at Lys56 of H3 (H3K56ac), a marker of newly synthesized histones[33] (Extended Data Fig. 1c). The replisome samples were cross-linked by GraFix and imaged using EM (Extended Data Fig. 2a). From the 2D average images, the overall architecture of the replisome particles resembles those of the in vitro reconstituted replisomes[22,23] (Extended Data Fig. 2b,c). Fuzzy densities were also observed immediately on top of Tof1–Csm3, indicating that the replisome front is highly dynamic. Given that the levels of FACT and histones in our samples are comparable to those of CMG in the replisome (Extended Data Fig. 1d), we speculate that the replisome front is where FACT engages with other replisome components and parental histones. We therefore performed deep three-dimensional (3D) classification focusing on the front end of the replisome and determined a stable structure of the FACT–histone complex bound to the replisome at an overall resolution of 3.5 Å (Extended Data Fig. 2d,e,j). Notably, this conformation accounts for only approximately 7% of the total replisome particles, highlighting a highly dynamic FACT–histone complex at the replication forks. The cryo-EM maps allowed for an unambiguous subunit assignment of FACT and histones, as well as model building for the middle domain (MD) and carboxyl-terminal domain (CTD) of Spt16 and six histone subunits in addition to other replisome components. Although the densities corresponding to Pob3 and the dimerization domain (DD) of Spt16 are of poorer quality (Extended Data Fig. 2f,k), the available models from the previous FACT–nucleosome structures[18,19] could be fitted well in the relevant regions.

Architecture of the endogenous replisome

In the replisome structure (Fig. 1), CMG, Tof1–Csm3, Ctf4, Polε and forked DNA are arranged in a manner similar to previously reported structures[23–25]. While the planar N-tier ring of Mcm2-7 remains relatively stable, its C-tier ring is dynamic (Extended Data Fig. 2h), suggesting that the C-tier motor region of the CMG helicase exists in multiple translocating states. Focused classification identified one relatively stable conformation of the C-tier ring. Notably, the stable attachment of Polε correlates well with the stability of the MCM (Mcm2-7 complex) CTD ring (Extended Data Fig. 2h,i). The Tof1–Csm3 heterodimer is assembled onto the N-tier face of the MCM ring over subunits Mcm2, 6, 4 and 7, with its top surface as a docking platform for the FACT–histone complex (Fig. 1). Consistent with previous studies[23,35], the density corresponding to Mrc1 is not obvious in the replisome, except for a small helix-containing region (residues 324–343) tightly attached to the side surface of Tof1 (Fig. 1a,b,d,e). The parental duplex DNA is

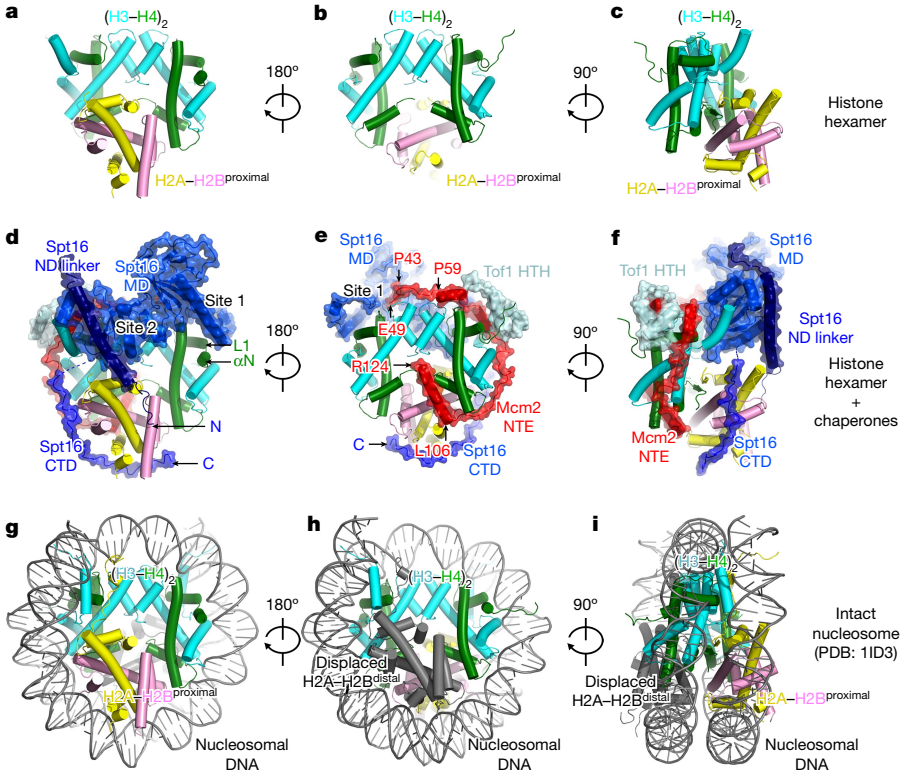

Fig. 2 | The evicted histone hexamer and its chaperones at the replication fork. a–c, The atomic model of the evicted histones shown as a cartoon presentation and displayed in three different views. **d–f**, The chaperone–histone complex captured at the replication fork is shown as a cartoon presentation with the surface presentation of Spt16, Mcm2 and Tof1 superimposed, displayed in three different views. C, C terminus; N, N terminus; ND linker, Spt16 NTD DD linker; site1/2, Spt16-MD-binding site 1/2. **g–i**, The atomic model of an intact nucleosome (Protein Data Bank (PDB): 1ID3) displayed in three different views.

stably anchored onto Tof1–Csm3 (Fig. 1c,f). Notably, FACT straddles the parental duplex DNA through the Spt16 DD, placing the Spt16 MD and Pob3 on opposite sides of the DNA (Fig. 1). This similar arrangement was also observed in FACT structures either with nucleosomes or RNA polymerases[17–19] (Extended Data Fig. 3a–j). On the side closer to Mcm4, Pob3 is flexibly hung onto the duplex DNA by interacting with the Spt16 DD through its own DD. On the opposite side, Spt16 joins hands with the Mcm2 NTE to chaperone the evicted histones at the replisome front (Figs. 1 and 2 and Extended Data Fig. 4).

Histone hexamer and its chaperones

A notable feature of our structure is the complete stripping of the duplex DNA off the histones (Fig. 1). The evicted histones are preserved in the form of a hexamer comprising one H3–H4 tetramer and one H2A–H2B^{proximal} dimer (proximal to Spt16 MD; Fig. 2a–f), adopting a conformation that is generally similar to that in an intact nucleosome (Fig. 2g–i and Extended Data Fig. 5a–c). The Spt16 MD directly binds to the lateral surface of the free H3–H4 tetramer on top of the four-helix bundle of the H3 dimer at two separate binding sites (Fig. 2 and Extended Data Figs. 4 and 5d), consistent with a crystal structure of the human SPT16 MD in a complex with the H3–H4 tetramer[36]. A substantial shift and rotation in the Spt16 MD was observed when compared with the available FACT–nucleosome structures[18,19] (Extended Data Fig. 3g–w), highlighting a major movement of Spt16 during substrate transition from nucleosome/subnucleosome to the free histone hexamer. The mode of the Spt16-MD–histone interaction in the replisome is also similar to those observed in transcription complexes[17] (Extended Data Fig. 3n–w), indicating a conserved role of FACT in handling nucleosome dynamics during both DNA replication and RNA transcription processes. At Spt16-MD-binding site 1 on the H3–H4 tetramer, acidic residues (residues 778–797) from the Spt16 MD are situated on the DNA-binding surfaces of the N-terminal helix (αN) and loop 1 (L1) of H4 to provide a shielding effect (Fig. 2d and Extended Data Fig. 4). At binding site 2, the Spt16 MD occupies the binding surface for the H2A-docking segment, and its $(H3–H4)_2$-binding loop further invades into the canonical binding site for the H2A–H2B^{proximal}, causing slight displacement of this dimer on the H3–H4 tetramer (Extended Data Fig. 5). To prevent H2A–H2B loss, the acidic CTD tail of Spt16 wraps around the H2A–H2B^{proximal}, occupying its exposed DNA-binding surface (Fig. 2d–i). Furthermore, one loop region extended from the long α helix of the Spt16's NTD DD linker engages with the H2A–H2B^{proximal} (Fig. 2d), reinforcing its tethering to the H3–H4 tetramer.

On the side of the H3–H4 tetramer that is originally occupied by the H2A–H2B^{distal} (distal to the Spt16 MD) in the nucleosome (Fig. 2), the relevant H2A–H2B-binding surface is occluded by the Mcm2 HBD (residues 49–124) through its long α helix (residues 106–124), which engages H4 in a manner similar to the human MCM2-HBD–H3–H4 structure[27] (Fig. 2 and Extended Data Fig. 6a,b). Notably, this helix also shows a weak interaction with H2A (Fig. 2e,h). Moreover, Mcm2 stretches its upstream segment (residues 59–105) to wrap around the DNA-binding surface of one H3–H4 dimer and further extends its N terminus (residues 49–58) across the tetramerization surface to the second H3–H4 dimer, covering the four-helix bundle between the H3 dimer (Fig. 2e and Extended Data Figs. 4 and 6). When approaching the Spt16-binding site 1 on the H3–H4 tetramer, Mcm2 makes a 90° turn away from H3 before becoming disordered (Fig. 2e and Extended Data Figs. 4a,e and 6a,b). In contrast to the human MCM2-HBD–H3–H4 structure, in which two MCM2 HBDs are associated with the H3–H4 tetramer symmetrically, the histone hexamer in the replisome accommodates the binding of

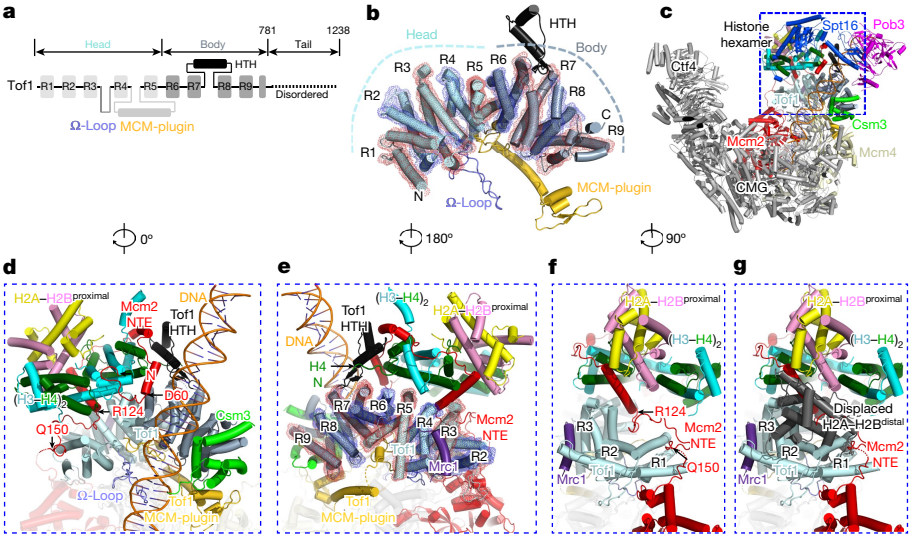

Fig. 3 | Deposition of the histone hexamer by Mcm2 NTE onto the top surface of Tof1. a, The domain organization of Tof1. R1–R9, the nine tandem helical repeats of Tof1. **b**, The structure of Tof1 from the replisome with its R1–R9 shown as a transparent surface presentation. **c**, The overall structure of the replisome, highlighting the position of FACT–histone at the replication fork. **d**–**f**, Magnified views of the boxed region in **c** with the indicated rotation. **g**, The same as in **f**, but with the displaced H2A–H2B^{distal} superimposed.

a single Mcm2 HBD (Fig. 2e and Extended Data Figs. 4 and 6a), as the configurations of FACT and H2A–H2B^{proximal} form steric hindrance to the binding of a second Mcm2 HBD (Extended Data Fig. 6c–e). This unique arrangement leaves a large portion of the DNA-binding surface on the second H3–H4 dimer unprotected.

Tof1 as a platform for histone transfer

In the replisome structure, Tof1 adopts a crescent-shaped conformation with a curvature mimicking the MCM ring on top of the N-tier face of Mcm2, 6, 4 and 7 (Figs. 1 and 3), in agreement with the reported structures[23,24,26,35]. The structured region of Tof1 contains nine tandem helical (2 or 3) repeats (R1–9) embedded with three insertion motifs including the Ω-loop, MCM-plugin and a unique helix-turn-helix (HTH)-containing motif (Fig. 3a,b). This region can be divided into head and body subdomains, which constitute distinct platforms for coordinating the docking of the evicted histones and the parental duplex DNA. As shown in Fig. 3c–f, the histone hexamer chaperoned by Spt16 and Mcm2 is deposited in a space right above the head region of Tof1. However, the parental DNA is anchored onto the surface of the Tof1's body region. This anchoring is further strengthened by Csm3 through its association with the C terminus of the Tof1 body region (Fig. 3d). Notably, Tof1's HTH motif is inserted as a wedge with two oppositely charged patches into the gap between the histones and DNA (Figs. 3a–e and 4a,f). The acidic patch (residues 642–653) from Tof1 HTH engages the αN and N-terminal tail of H4, while its upstream flanking loop containing a basic patch (residues 615–622) makes contacts with the nearby DNA backbone (Fig. 3d,e). Through these interactions, Tof1 separates the evicted histones from the parental duplex DNA.

Although the evicted histones are situated over the head region of Tof1, they did not form a close contact. Instead, the docking of the FACT–histone complex onto Tof1 is largely mediated by the Mcm2 NTE (residues 60–150) as a cushion (Fig. 3d–f), which includes its HBD (residues 60–124) and a linker region (residues 125–150, Mcm2-L) between its HBD and NTD to engage Tof1 at four major sites (Figs. 3 and 4). At docking site 1, residues 141–150 of Mcm2-L are embedded into the cleft between the two helices of Tof1 R1 (residues 11–70) through hydrophobic interactions and a few hydrogen interactions (Fig. 4a,c,g,k). At docking site 2, the acidic patch (residues 130–137, DDEDEEQE) of Mcm2-L is situated on a positively charged surface formed by four basic residues (Lys56, Lys59, Lys63, Arg197) and one polar residue (Gln130) from R1–3 of Tof1 (Fig. 4a,b,d,h,l). Docking site 3 involves the interactions between the hydrophobic loop (residues 126–129) and long helix of the Mcm2 NTE and the residues from Tof1 R2–4 (Fig. 4a,e,i,m,n). At docking site 4, the 68–89 region of the Mcm2 HBD also makes extensive contacts with the HTH-containing region of Tof1 (Fig. 4a,b,f,j). Together, these interactions between the Mcm2 NTE and Tof1 relocate the detached histones temporarily to the replisome front. Notably, these interactions between Tof1 and the Mcm2 NTE were not observed in other replisome structures that do not include the FACT–histone complex[23,24,26,37].

Parental histone recycling via Mcm2–Tof1 coupling

To investigate the role of the Mcm2-NTE–Tof1 interaction during parental histone transfer, we performed enrichment and sequencing of protein-associated nascent DNA (eSPAN) analysis[33,38] to monitor the distribution of both parental and newly synthesized histones on the leading and lagging strands at replication forks in cells bearing relevant *mcm2* or *tof1* mutants (Fig. 5a and Methods). In particular, key residues from the Mcm2-NTE–Tof1 interfaces were either mutated or deleted to disturb the interaction between Mcm2 and Tof1.

Our eSPAN analysis with *tof1-3A* mutant cells, in which three key residues (Arg60, Arg197, Asp280) from the Mcm2-NTE–Tof1 interface were replaced with alanine (Fig. 4k,l,n), shows an apparent leading-strand bias for H3K4me3 eSPAN signals (Fig. 5b,c,h and Extended Data Fig. 7a) and a correlated lagging-strand bias for H3K56ac eSPAN signals (Extended Data Figs. 7a and 8a–c,g), highlighting a defect in parental histone transfer to the lagging strand when the binding of the Mcm2 NTE to Tof1 is disturbed. This observation is consistent with the fact that Tof1 is located at the replisome front in a strategic position proximal to the newly synthesized lagging strand. We also tested the impact of removing the unique HTH-containing motif (residues 612–656) from Tof1 (*tof1-ΔHTH*). Notably, we did not observe a bias in H3K4me3 eSPAN signals (Fig. 5b,c,h), suggesting that deletion of the Tof1 HTH has no apparent effect on parental histone transfer. However, it is also possible that the removal of the Tof1 HTH may equally affect parental histone recycling at both the leading and lagging strands, which cannot be detected by the eSPAN bias. To differentiate these possibilities, we calculated the H3K4me3 eSPAN densities within a 2 kb region around

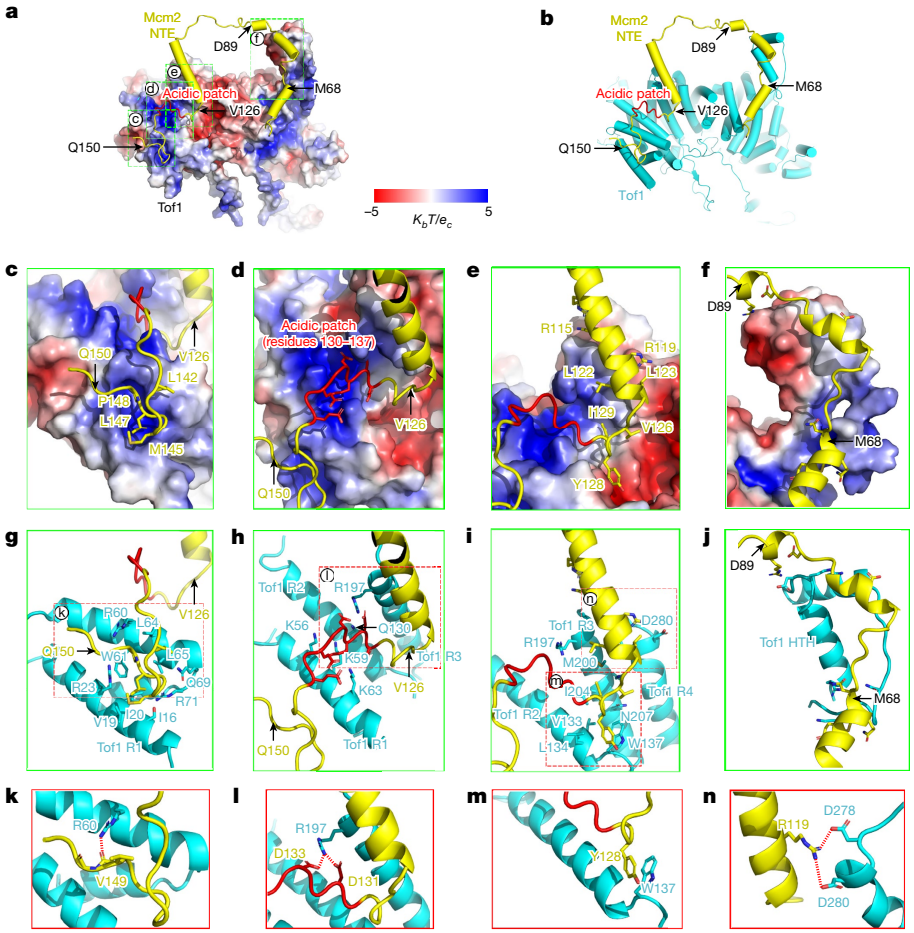

Fig. 4 | The detailed interactions between the Mcm2 NTE and Tof1. **a**,**b**, Overview of the interaction between the Mcm2 NTE (yellow) and Tof1 (cyan in **b**) for mediating the histone docking, shown as an electrostatic surface potential (K_bT/e_c) map of Tof1 (**a**) and as a cartoon presentation (**b**). The acidic patch (residues 130–137) of the Mcm2 NTE is highlighted in red. **c**–**f**, Magnified views of the regions indicated by boxes in **a**. The key residues of Mcm2 involved in the Mcm2–Tof1 interaction are shown and labelled. **g**–**j**, The same as in **c**–**f**, but with Tof1 shown as a cartoon presentation. The key residues from the Mcm2–Tof1 interfaces are shown, and only those from Tof1 are labelled. **k**–**n**, Magnified views of the regions indicated by boxes in **g**–**i**. **k**, The hydrogen bonding between the carboxy oxygen from the backbone of Mcm2 Val149 and the guanidinium group of Tof1 Arg60. **l**, Charge–charge interactions between Asp131 and Asp133 of Mcm2 and Arg197 of Tof1. **m**, Tyr128 of Mcm2 is inserted into a hydrophobic pocket formed by Val133, Leu134 and Trp137 from Tof1 R2–3. **n**, Mcm2 Arg119 makes charge–charge interactions with Asp278 and Asp280 of Tof1.

ARS (autonomous replication sequence) consensus sequence (ACS) locations between wild-type (WT) and mutant strains (Fig. 5d). We found that the H3K4me3 density signals at early replication origins were noticeably reduced at the lagging strands in *tof1-3A* cells compared with those in the WT cells, suggesting that parental histone recycling around early replication origins is impaired after disruption of the interactions between Tof1 and the Mcm2 NTE. By contrast, we did not observe an obvious reduction in the H3K4me3 signals in the *tof1-ΔHTH* cells (Fig. 5d), except a subtle preference of H3K56ac-eSPAN signals toward lagging strands (Extended Data Fig. 8a). This bias appears to be relatively minor compared with the pronounced bias observed in *tof1-3A* and other mutant cells (Extended Data Fig. 8a,d). Nevertheless, the effects of the *tof1-ΔHTH* mutant on both H3K56ac and H3K4me3 are very similar to those of the WT cells (Extended Data Fig. 8c). These results suggest that the docking of the Mcm2 NTE onto Tof1 is crucial for the recycling of parental histones to the lagging strand at the replication fork, and the binding of Mcm2 to the Tof1 HTH motif may be dispensable during this process.

To obtain further evidence, we performed eSPAN analyses with two *mcm2* mutants, *mcm2-6A* (R119A, Y128A, I129A, D131A, E135A, E137A) in which six key residues of Mcm2 from the interfaces between the Mcm2 NTE and Tof1 were mutated to alanine (Fig. 4l–n), and *mcm2ΔL* in which the linker region (residues 126–150) of the Mcm2 NTE docked on the surface of Tof1 R1–3 was deleted (Fig. 4a–e,g–i,k–n). With these mutants, we also detected an apparent leading-strand bias for H3K4me3 eSPAN signals (Fig. 5e,f,g,i and Extended Data Fig. 7a) in addition to their corresponding lagging-strand bias for H3K56ac eSPAN signals (Extended Data Fig. 8d–f,h). In fact, the eSPAN bias associated with *mcm2-6A* is more significant than that of *mcm2ΔL*, suggesting that the Mcm2-NTE–Tof1 coupling mediated by both Mcm2-L and the long α-helix of the Mcm2 HBD contributes to parental histone transfer at the replication forks.

To rule out the biased distribution of H3K4me3 or H3K56ac at nascent chromatin in the relevant *tof1* and *mcm2* mutants as a result of defects in DNA replication, we further analysed the correlation between the H3K4me3 or H3K56ac eSPAN bias and the 5-bromo-2-deoxyuridine (BrdU)-incorporation level at each early replication origin. Our results show little or no correlation between these two parameters in WT and mutant cells (Extended Data Fig. 9). Moreover, the profiles of S phase progression, as measured by flow cytometry analysis of DNA content (Extended Data Fig. 7b), were similar in WT and mutant cells. Taken together, these results unravel a unique role of Mcm2–Tof1 coupling in directing the parental histone transfer to the lagging strand at replication forks.

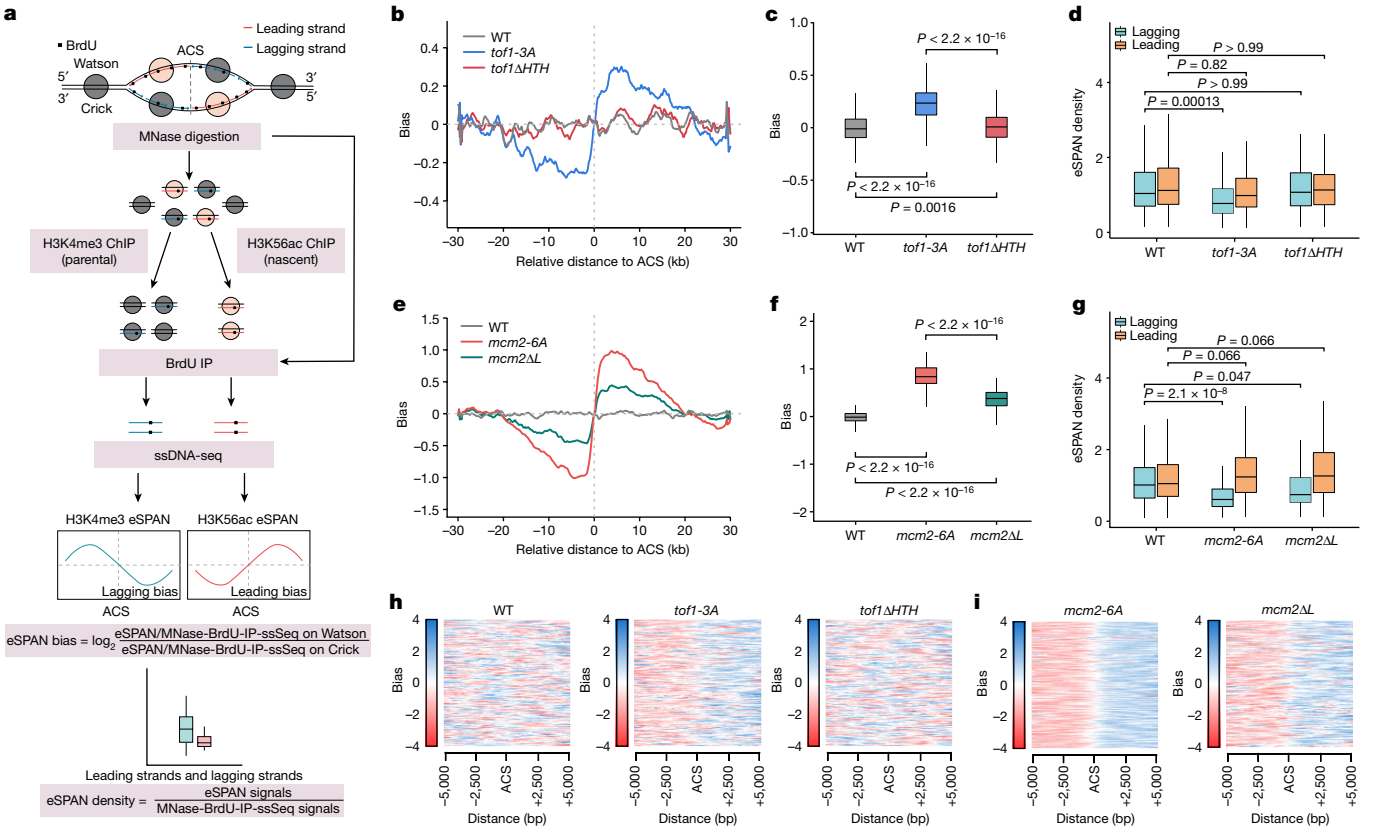

Fig. 5 | eSPAN analyses of parental histone recycling mediated by the interaction between Tof1 and the Mcm2 NTE. a, Illustration of the eSPAN experimental workflow and data analysis process. ssDNA-seq, single-stranded DNA sequencing. **b**, Line plots of the H3K4me3-eSPAN bias show the relative amount of parental histone transfer between the two daughter strands in WT, *tof1-3A* (R60A/R197A/D280A) and *tof1ΔHTH* (Δ612–656aa) cells. The H3K4me3-eSPAN bias around 139 early replication origins of the ACSs was calculated. **c**, The H3K4me3-eSPAN bias around the 139 ACSs in WT, *tof1-3A* and *tof1ΔHTH* mutant cells. $n = 139$. **d**, The H3K4me3-eSPAN density on both leading and lagging strands in WT, *tof1-3A* and *tof1ΔHTH* cells. $n = 139$. The comparison of eSPAN density between WT and mutant cells was assessed using rank-sum Wilcoxon tests. **e**, Line plots of the H3K4me3-eSPAN bias around the 139 ACSs in WT, *mcm2-6A* (R119A/Y128A/I129A/D131A/E135A/E137A) and *mcm2ΔL* (Δ126–150aa) cells are shown. **f**, The H3K4me3-eSPAN bias around the 139 ACSs in WT, *mcm2-6A* and *mcm2ΔL* mutant cells are shown. **g**, The H3K4me3-eSPAN density on both leading and lagging strands in WT, *mcm2-6A* and *mcm2ΔL* cells. **h**,**i**, The H3K4me3-eSPAN bias around 139 ACSs in WT, *tof1-3A* and *tof1ΔHTH* (**h**), and *mcm2-6A* and *mcm2ΔL* (**i**) cells. The box plots in **c**, **d**, **f** and **g** show the median value (centre line), minimum and maximum values (whiskers), and 25% and 75% quartiles (box limits). *P* values were calculated using two-sided rank-sum Wilcoxon tests. Similar results were obtained in two independent experiments. See the Methods for more details.

Discussion

Here we determined the cryo-EM structures of the endogenous replisomes isolated from early-S-phase cells and captured a key step of the replication-coupled histone transfer at replication forks (Fig. 6). Our findings suggest that the histone octamer from a parental nucleosome was first split into one H2A–H2B^{proximal}–(H3–H4)$_2$ hexamer and one H2A–H2B^{distal} dimer during nucleosome disassembly at the replication fork. The evicted histone hexamer was chaperoned by Spt16, Mcm2 and Tof1, and deposited to the replisome front over the head region of Tof1. At this stage, Spt16 makes extensive contacts with the histone hexamer, stably tethering the H2A–H2B^{proximal} dimer to the H3–H4 tetramer. We did not observe the displaced H2A–H2B^{distal} dimer, which may remain associated with certain floppy acidic motif(s) from FACT or replisome component(s) or may be released during the nucleosome-disassembly process. Given that SSRP1 (the human homologue of Pob3) can destabilize H2A–H2B^{distal} from the histone octamer[19], we speculate that the removal of H2A–H2B^{distal} is a crucial step during histone recycling, as it is required for the binding of the Mcm2 HBD to the histone hexamer, and this arrangement also secures a proper docking of the FACT–histone complex onto Tof1. It is probable that the evicted histone hexamer could be recycled as a unit to the daughter strands (Fig. 6).

Consistent with this idea, both new and old H2A–H2B can be found associated with the old parental H3–H4 tetramer as a 'hybrid nucleosome' at daughter strands[39]. A recent study also showed that parental H2A–H2B dimer is recycled symmetrically and accurately to daughter strands in mouse embryonic stem cells using a mechanism that is different from that of H3–H4 recycling[34]. With the structural information from our study, we speculate that both old H2A–H2B dimers could be recycled but through different pathways: (1) the old H2A–H2B^{proximal} is recycled through its association with the old H3–H4 tetramer in the form of a hexamer, and (2) the old H2A–H2B^{distal} is reused through a redundant pathway independent of the parental H3–H4. If the second pathway does exist, the displaced H2A–H2B^{distal} must be captured and transferred to the daughter strands by some factor(s) such as POLA1[34]. At present, we cannot rule out the possibility that the parental histone hexamer may be further split into one H2A–H2B^{proximal} and one H3–H4 tetramer in a downstream process. Previous studies suggested that the histone chaperone ASF1 cooperates with the HBD of human MCM2 to recycle the H3–H4 dimers[27,28,40]. Our observation that an intact H3–H4 tetramer as the intermediate is associated with the replisome at the fork does not support the involvement of Asf1 or any related factors in H3–H4 dimer recycling. However, it is still possible that Asf1 has a role in a later stage of the process. Moreover, Asf1 may work together with the Mcm2 HBD under stressed conditions. To fully unravel the

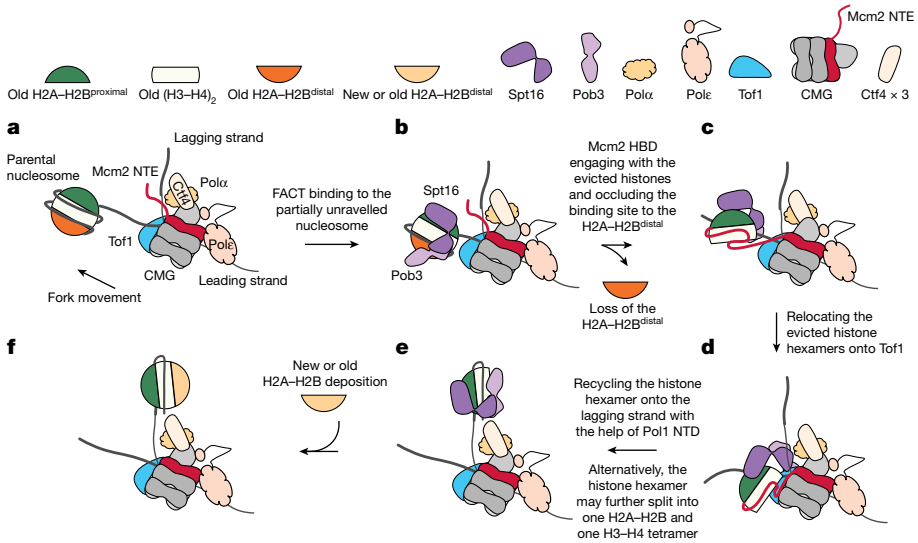

Fig. 6 | Model of parental histone recycling to the lagging strand mediated by the replisome and FACT at the replication fork. a,**b**, During replication fork progression (**a**), FACT first recognizes and binds to the partially unravelled nucleosome (**b**). This binding may destabilize the H2A–H2B^{distal} binding to the H3–H4 core. **c**, With the dissociation of the H2A–H2B^{distal} and further exposure of H3–H4, Spt16 and the Mcm2 HBD are allowed to fully engage with the remaining histones. **d**, Once fully evicted from the DNA, the histone hexamer is transferred and docked onto the head region of Tof1 through the interaction between the Mcm2 NTE and Tof1. **e**, This relocation paves the way for the recycling of the histone hexamer to the lagging strand. The subsequent transfer may involve the interplay between Polα, the Mcm2 HBD and FACT to deposit the parental histone hexamer to the newly synthesized lagging strand DNA, resulting in the formation of a hexasome. Alternatively, the histone hexamer may further split. **f**, Finally, nucleosome reassembly is accomplished with the incorporation of new and/or old H2A–H2B dimer(s) and the departure of FACT from the nucleosome complex.

mechanisms of parental histone recycling, further studies are needed to capture relevant intermediates at replication forks.

In the replisome structure, the configuration of the Spt16 MD on the histone hexamer determines where the Mcm2 HBD can bind to the H3–H4 tetramer (Extended Data Fig. 6). As a result, the DNA-binding surfaces of the other H3–H4 dimer facing Ctf4 are not fully covered. We believe that the exposed surfaces may have important implications for histone recycling. For example, they could provide entry points for other chaperone(s), such as Polα, to capture the evicted histones. A recent cryo-EM structure of the in vitro reconstituted replisome containing the Polα–primase complex showed that Polα is targeted onto the replisome at a location between Ctf4 and the FACT–histone-binding sites[37] (Fig. 6). In this structure, the flexible NTD of Pol1 containing a histone-binding motif is situated at a strategic location through its binding to Ctf4. This arrangement could enable the Pol1 NTD to easily bind to the exposed surfaces of the H3–H4 tetramer to ensure an efficient and precise handover of the parental histones.

It is known that histone recycling to the leading strand requires the involvement of Polε[33]. Our analyses of the endogenous replisomes identified two major conformations of Polε: (1) a stable Polε engaging with the motor domain of CMG helicase, and (2) a highly flexible Polε attached to the CMG through the NTD of Dpb2. We speculate that Polε might participate in parental histone recycling through alternating between these two states. When Polε disengages from the MCM ring, it could use the Dpb2 NTD as a hinge to flip over the helicase to the fork front, where Dpb3 and Dpb4 could capture the FACT–histone complex[26]. The binding of Polε to the MCM ring may facilitate the deposition of the captured histones onto the leading-strand DNA. This process may require some replisome components to participate and cooperate with Spt16 to chaperone the evicted histones. It is not clear whether this process involves Tof1 as a similar platform for histone recycling to the leading strand. Tof1 has two available surfaces (top and side) for recruiting FACT–histone complexes at the fork front. We envision that the side surface of Tof1 may facilitate the docking of FACT–histone destined for transfer to the leading strand. Notably, Mrc1 is attached to the side surface of Tof1[23,24] (Fig. 1). Further investigations are needed to determine the roles of Tof1 in histone recycling as well as whether Mrc1 and its coupling to Tof1 contribute to this process.

In summary, this study provides a key snapshot of how the parental histones are transferred at replication forks. It also lays a solid foundation for future directions to unravel the mechanism that couples histone-encoded epigenetic information transfer with DNA replication.

Online content

Any methods, additional references, Nature Portfolio reporting summaries, source data, extended data, supplementary information, acknowledgements, peer review information; details of author contributions and competing interests; and statements of data and code availability are available at https://doi.org/10.1038/s41586-024-07152-2.

1. Zhou, K., Gaullier, G. & Luger, K. Nucleosome structure and dynamics are coming of age. *Nat. Struct. Mol. Biol.* **26**, 3–13 (2019).
2. Sekine, S. I., Ehara, H., Kujirai, T. & Kurumizaka, H. Structural perspectives on transcription in chromatin. *Trends Cell Biol.* https://doi.org/10.1016/j.tcb.2023.07.011 (2023).
3. Yung, P. Y. K. & Elsasser, S. J. Evolution of epigenetic chromatin states. *Curr. Opin. Chem. Biol.* **41**, 36–42 (2017).
4. Du, W. et al. Mechanisms of chromatin-based epigenetic inheritance. *Sci. China Life Sci.* **65**, 2162–2190 (2022).
5. Stewart-Morgan, K. R., Petryk, N. & Groth, A. Chromatin replication and epigenetic cell memory. *Nat. Cell Biol.* **22**, 361–371 (2020).
6. Zhang, W., Feng, J. & Li, Q. The replisome guides nucleosome assembly during DNA replication. *Cell Biosci.* **10**, 37 (2020).
7. Shan, Z. et al. The patterns and participants of parental histone recycling during DNA replication in *Saccharomyces cerevisiae*. *Sci. China Life Sci.* **66**, 1600–1614 (2023).
8. Attali, I., Botchan, M. R. & Berger, J. M. Structural mechanisms for replicating DNA in eukaryotes. *Annu. Rev. Biochem.* **90**, 77–106 (2021).
9. Bell, S. P. & Labib, K. Chromosome duplication in *Saccharomyces cerevisiae*. *Genetics* **203**, 1027–1067 (2016).
10. Yao, N. Y. & O'Donnell, M. E. The DNA replication machine: structure and dynamic function. *Subcell. Biochem.* **96**, 233–258 (2021).
11. Gao, Y. & Yang, W. Different mechanisms for translocation by monomeric and hexameric helicases. *Curr. Opin. Struct. Biol.* **61**, 25–32 (2020).
12. Yeeles, J. T. P., Janska, A., Early, A. & Diffley, J. F. X. How the eukaryotic replisome achieves rapid and efficient DNA replication. *Mol. Cell* **65**, 105–116 (2017).
13. Kurat, C. F., Yeeles, J. T. P., Patel, H., Early, A. & Diffley, J. F. X. Chromatin controls DNA replication origin selection, lagging-strand synthesis, and replication fork rates. *Mol. Cell* **65**, 117–130 (2017).

14. Yeeles, J. T., Deegan, T. D., Janska, A., Early, A. & Diffley, J. F. Regulated eukaryotic DNA replication origin firing with purified proteins. *Nature* **519**, 431–435 (2015).
15. Formosa, T. The role of FACT in making and breaking nucleosomes. *Biochim. Biophys. Acta* **1819**, 247–255 (2013).
16. Safaric, B. et al. The fork protection complex recruits FACT to reorganize nucleosomes during replication. *Nucleic Acids Res.* **50**, 1317–1334 (2022).
17. Ehara, H., Kujirai, T., Shirouzu, M., Kurumizaka, H. & Sekine, S. I. Structural basis of nucleosome disassembly and reassembly by RNAPII elongation complex with FACT. *Science* **377**, eabp9466 (2022).
18. Farnung, L., Ochmann, M., Engeholm, M. & Cramer, P. Structural basis of nucleosome transcription mediated by Chd1 and FACT. *Nat. Struct. Mol. Biol.* **28**, 382–387 (2021).
19. Liu, Y. et al. FACT caught in the act of manipulating the nucleosome. *Nature* **577**, 426–431 (2020).
20. Georgescu, R. et al. Structure of eukaryotic CMG helicase at a replication fork and implications to replisome architecture and origin initiation. *Proc. Natl Acad. Sci. USA* **114**, E697–E706 (2017).
21. Douglas, M. E., Ali, F. A., Costa, A. & Diffley, J. F. X. The mechanism of eukaryotic CMG helicase activation. *Nature* **555**, 265–268 (2018).
22. Sun, J. et al. The architecture of a eukaryotic replisome. *Nat. Struct. Mol. Biol.* **22**, 976–982 (2015).
23. Baretić, D. et al. Cryo-EM structure of the fork protection complex bound to CMG at a replication fork. *Mol Cell* **78**, 926–940 (2020).
24. Jones, M. L., Baris, Y., Taylor, M. R. G. & Yeeles, J. T. P. Structure of a human replisome shows the organisation and interactions of a DNA replication machine. *EMBO J.* **40**, e108819 (2021).
25. Rzechorzek, N. J., Hardwick, S. W., Jatikusumo, V. A., Chirgadze, D. Y. & Pellegrini, L. CryoEM structures of human CMG-ATPγS-DNA and CMG-AND-1 complexes. *Nucleic Acids Res.* **48**, 6980–6995 (2020).
26. Xu, Z. et al. Synergism between CMG helicase and leading strand DNA polymerase at replication fork. *Nat. Commun.* **14**, 5849 (2023).
27. Huang, H. et al. A unique binding mode enables MCM2 to chaperone histones H3-H4 at replication forks. *Nat. Struct. Mol. Biol.* **22**, 618–626 (2015).
28. Wang, H., Wang, M., Yang, N. & Xu, R. M. Structure of the quaternary complex of histone H3-H4 heterodimer with chaperone ASF1 and the replicative helicase subunit MCM2. *Protein Cell* **6**, 693–697 (2015).
29. Evrin, C., Maman, J. D., Diamante, A., Pellegrini, L. & Labib, K. Histone H2A-H2B binding by Pol α in the eukaryotic replisome contributes to the maintenance of repressive chromatin. *EMBO J.* https://doi.org/10.15252/embj.201899021 (2018).
30. Li, Z. et al. DNA polymerase α interacts with H3-H4 and facilitates the transfer of parental histones to lagging strands. *Sci. Adv.* **6**, eabb5820 (2020).
31. Petryk, N. et al. MCM2 promotes symmetric inheritance of modified histones during DNA replication. *Science* **361**, 1389–1392 (2018).
32. Gan, H. et al. The Mcm2-Ctf4-Polα axis facilitates parental histone H3-H4 transfer to lagging strands. *Mol. Cell* **72**, 140–151 (2018).
33. Yu, C. et al. A mechanism for preventing asymmetric histone segregation onto replicating DNA strands. *Science* **361**, 1386–1389 (2018).
34. Flury, V. et al. Recycling of modified H2A-H2B provides short-term memory of chromatin states. *Cell* **186**, 1050–1065 (2023).
35. Jenkyn-Bedford, M. et al. A conserved mechanism for regulating replisome disassembly in eukaryotes. *Nature* **600**, 743–747 (2021).
36. Tsunaka, Y., Fujiwara, Y., Oyama, T., Hirose, S. & Morikawa, K. Integrated molecular mechanism directing nucleosome reorganization by human FACT. *Genes Dev.* **30**, 673–686 (2016).
37. Jones, M. L., Aria, V., Baris, Y. & Yeeles, J. T. P. How Pol α-primase is targeted to replisomes to prime eukaryotic DNA replication. *Mol. Cell* **83**, 2911–2924 (2023).
38. Yu, C. et al. Strand-specific analysis shows protein binding at replication forks and PCNA unloading from lagging strands when forks stall. *Mol. Cell* **56**, 551–563 (2014).
39. Xu, M. et al. Partitioning of histone H3-H4 tetramers during DNA replication-dependent chromatin assembly. *Science* **328**, 94–98 (2010).
40. Groth, A. et al. Regulation of replication fork progression through histone supply and demand. *Science* **318**, 1928–1931 (2007).

Methods

Yeast strain

All of the yeast strains that were used in this study were derivatives of the W303 (leu2-3, 112 ura3-1 his3-11, trp1-1, ade2-1 can1-100) genetic background (Supplementary Table 2). Strain Y277 for replisome purification was constructed using a one-step PCR-based approach with pTF272 (pFA6a-TEV-6xGly-3×Flag-HphMX, Addgene) as DNA template to generate the PSF2-3×Flag tagging modification in the W303-1a background strain. Strains for eSPAN analyses were generated using the CRISPR–Cas9 plasmid pML104 along with the primers described in Supplementary Table 3.

Replisome purification

To isolate the endogenous replisomes for structural determination, 100 liters of log-phase (optical density at 600 nm (OD_{600}) of 2.0) yeast cells (Y277, *PSF2-3×Flag*) were first synchronized at G1 phase with alpha factor (12.5 ng ml^{-1}), followed by washing once with fresh YPD medium before being released into fresh medium containing hydroxyurea (200 mM) for 1.5 h. Cells were collected and washed with buffer I (50 mM HEPES-KOH pH 7.5, 150 mM L-glutamic acid potassium salt, 8 mM $MgCl_2$, 1 mM EDTA, 0.02% NP-40, 3 mM ATP, 2 mM NaF, 1 mM phenylmethanesulfonylfluoride (PMSF) and 1× protease inhibitor cocktail (Roche). The cell pellets were resuspended in 0.5 volumes of buffer I. The cell suspension was frozen drop-wise in liquid nitrogen and then disrupted with a freezer mill (SPEX CertiPrep 6850 Freezer/Mill). The cell powder was thawed on ice by adding an equal volume of buffer I to obtain the insoluble crude chromatin, followed by washing once with buffer I. To solubilize chromatin-bound replisomes, the crude chromatin was digested in buffer I containing benzonase (0.5 U μl^{-1}; 7sea biotech, RPE002) for 10 min at 37 °C, and then 1 h on ice. The suspension was then centrifuged for 20 min at 38,900*g*. The clear phase was recovered and subjected to anti-Flag immunoprecipitation (IP) with anti-Flag M2 Affinity Gel (Sigma-Aldrich, A2220) at 4 °C for 3 h. The beads were recovered and washed extensively with buffer II (50 mM HEPES-KOH pH 7.5, 150 mM KOAc, 8 mM $MgCl_2$, 1 mM EDTA, 2 mM NaF, 1 mM PMSF). The precipitated replisomes were eluted with 0.5 mg ml^{-1} of 3×Flag peptide (GenScript, U6320GJ210-1) in buffer II at 4 °C. The eluates were combined and concentrated. The replisome samples were then applied on top of a 20–40% glycerol gradient containing glutaraldehyde (0–0.16%) for cross-linking in buffer II. The glycerol gradients were centrifuged in a TLS-55 rotor (Beckman Optima MAX-XP Ultracentrifuge) at 77,100*g* for 9 h. The fractions were collected and the cross-linking reaction was quenched by addition of Tris-HCl (pH 7.5) buffer to a final concentration of 40 mM. The fractions containing the replisomes were pooled and processed for EM analyses. Ultrafiltration for the removal of glycerol, buffer exchange and sample concentration was performed with buffer II using a centrifugal filter (Amicon Ultra, 0.5 ml, 50 kDa) at 6,000*g* at 4 °C.

EM analysis

For negative staining, the samples were stained with 2% (w/v) uranyl acetate and examined using the Talos L120C microscope (Thermo Fisher Scientific) operated at 120 kV to determine the sample quality and estimate the relative concentration of samples used for cryo-grid preparation.

For cryo-grid preparation, 4 µl aliquots of samples were applied to a glow-discharged holey carbon grid (C-flat R 1.2/1.3 Au) and plunge frozen into liquid ethane cooled by liquid nitrogen using the Vitrobot VI (Thermo Fisher Scientific) after 3 s blotting with filter paper at 4 °C and under 100% humidity.

The grids were loaded onto an FEI Titan Krios G3i transmission electron microscope operated at 300 kV. Images were recorded on a Gatan K3 summit direct electron detector and a Bio Quantum energy filter with a 20 eV slit width. Images with a total dose of 50 e^{-} $Å^{-2}$ were acquired within 4 s at a nominal magnification 81,000× (EFTEM mode), corresponding to a calibrated pixel size of 1.06 Å. The dose was fractionalized to 40 frames equally. The defocus range was set between −1.0 and −2.5 µm. EPU (v.2.12) was used for data collection.

Data processing

In total, 9,537 movie stacks were collected for the samples of the endogenous replisome and were preprocessed in RELION (v.4.0)[41]. The super-resolution movie stacks underwent local drift correction, electron-dose weighting and twofold binning using MotionCor2 (v.1.4)[42]. This process generated both dose-weighted and unweighted summed micrographs. The unweighted version of micrographs was used for contrast transfer function (CTF) estimation, particle picking and coarse 2D/3D classification. On the other hand, the dose-weighted micrographs were used for fine 3D classification and map refinement. CTF estimation was performed using CTFFIND4[43]. Approximately 600 micrographs with high contrast were selected and processed for multiple rounds of manual/auto particle picking as well as initial 2D/3D classification to prepare accurate templates for particle auto-picking across the whole dataset. The auto-picking process was meticulously optimized using both the RELION template-matching method and the Topaz (v.0.2.5) deep-learning method[44,45].

A total of 1,542,000 particles was auto-picked from all of the micrographs and underwent initial 3D classification to exclude noise and bad particles (Extended Data Fig. 2d). From this analysis, 524,000 qualified particles were retained and processed for global refinement, which resulted in a 3.7 Å global density map. On the basis of this global map, the local densities of Spt16-MD–histone, Spt16-DD–Pob3, Ctf4 trimer, MCM CTDs and Polε were further enhanced through a cascade of mask-based local 3D classification and refinement steps (Extended Data Fig. 2e–i). All of the local classification procedures were performed in RELION with the '--skip_alignment' option enabled. For the region of Spt16-MD–histone, three subgroups (108,000 particles) showing high occupancy and improved structural features after local classification were combined and processed for multiple sequential refinement steps using either RELION or cryoSPARC (v.4.0) with gradually narrowed masks. This process resulted in a final local density map for the region of Spt16-MD–histone–Tof1 at a resolution of 3.5 Å (Extended Data Fig. 2e,i). Local 3D classification focused on the region of Spt16-DD–Pob3 was further applied on the optimized dataset of Spt16-MD–histone (108,000 particles), yielding two subgroups (15,000 and 16,000 particles) that showed improved structural features for the relevant density (Extended Data Fig. 2f). It is evident the state II Spt16-DD–Pob3 exhibits a minor shift away from the Tof1–Csm3 platform compared with state I. Notably, the structures of the state I Spt16-DD–Pob3 are shown in Fig. 1 and Extended Data Fig. 3. For the region of Ctf4, the particles showing low resolution or low Ctf4 occupancy were removed through local classification, leaving 232,000 particles for refining the local density map of Ctf4 using cryoSPARC, resulting in a map with a resolution at 3.5 Å (Extended Data Fig. 2g). Local 3D classification focused on the CTDs of the MCM ring led to the identification of two conformations, conformation-1 (72,000 particles) and conformation-2 (246,000 particles). After global refinement using cryoSPARC, the final resolutions of the maps of these two structures reached 3.8 Å (Extended Data Fig. 2h). As a stable Polε is associated with conformation-1, a local classification focused on the region of Polε was performed to improve the local resolution of Polε (Extended Data Fig. 2i). A composite global density map was generated using phenix.combine_focused_maps[46]. It consists of the densities of CMG, the CMG-bound DNA region from the global structure of Conformation-1, Tof1–Csm3–Mrc1–Spt16-MD–Mcm2-NTE–histone, their bound DNA region from the 3.5 Å Spt16-MD–histone–Tof1 locally optimized map, and Spt16-DD–Pob3 from the locally optimized map of Spt16-DD–Pob3 (state I), Ctf4 from the Ctf4 trimer local map, and Polε–Mcm5-WHD from the Polε locally optimized map. The local resolutions

of the composite map (Extended Data Fig. 2k) were calculated using the RELION's own local resolution estimation tool, based on the two composite half maps generated by phenix.combine_focused_maps. Chimera[47], ChimeraX[48] and PyMOL (v.2.5 Schrödinger) were used for figure preparation.

Model building

The cryo-EM structures of yeast CMG–Ctf4–Tof1–Csm3–fork-DNA complex (PDB: 6SKL), yeast RNA polymerase II–Spt4/5–nucleosome–FACT (PDB: 7NKY), yeast intact nucleosome (PDB: 1ID3) and human MCM2-HBD–$(H3–H4)_2$ complex (PDB: 5BNV) were used as initial models for model building. Predicted initial models from the AlphaFold Protein Structure Database[49] were used for Polε and WH domain of Mcm5. The domains or segments of the initial models were rigid-body fitted into the cryo-EM density maps of the replisome using ChimeraX (v.1.3)[48] and manually adjusted against the locally optimized density maps in Coot (v.0.9.8.92)[50]. For the region of Spt16-DD–Pob3, the atomic models of Spt16-DD–Pob3-DD and Pob3-MD from the reported structure (PDB: 7NKY) were rigid-body fitted into the locally optimized map of Spt16-DD–Pob3 (state I), separately, without manual adjustment. Given the low resolution, the side chains of the Spt16-DD–Pob3 regions were removed. The model of the N-terminal loop of Spt16 ND linker was de novo built using the main chain backbone without assigning any side chain due to the limit of the local resolution. The model of the Spt16 CTD was manually built by referencing the positioning of Spt16 CTD in previously reported FACT–histone structures (PDB: 6UPK, 7NKY, 7XTI). The model of most of its CTD sequence was also built using only the main chain backbone, except for residues 969–974, where the side chains can be properly assigned. The assignment of the relevant side chains was further confirmed by the structure prediction of the Spt16–H3–H4 complex using Alphafold2.

The merged atomic model was further refined against the composite global density map using phenix.real_space_refine[46] to optimize the overall geometry quality. The quality of the deposited model was evaluated using phenix.molprobity[51].

MS sample preparation

For MS analysis, the eluted replisome sample was fractionated using 20–40% glycerol gradient without glutaraldehyde cross-linking. The fractions containing replisomes were then resolved on a 4–12% Bis-Tris gel, followed by fixation in a 50% methanol/7% acetic acid solution. The gel was stained by GelCode Blue stain (Pierce), diced into 1 mm^3 cubes and destained by incubating with 50 mM ammonium bicarbonate/50% acetonitrile for 1 h. The destained gel cubes were dehydrated in acetonitrile for 10 min and rehydrated in 25 mM NH_4HCO_3 with trypsin for protein digestion at 37 °C overnight. The resultant peptides were enriched with StageTips. The eluted peptides were dried down using the SpeedVac and resuspended in 0.1% formic acid for analysis using liquid chromatography coupled with tandem MS (LC–MS/MS).

MS data analysis

The LC–MS/MS analysis of the replisome sample was performed on the Q Exactive Plus Hybrid Quadrupole-Orbitrap Mass Spectrometer (Thermo Fisher Scientific). The peptide samples in 0.1% formic acid were pressure loaded, rinsed for 5 min with 0.1% formic acid and subsequently eluted with a linear gradient from 4% B (96% A) to 35% B (65% A) in 90 min (A = 0.1% formic acid; B = 0.1% formic acid in 80% acetonitrile; flow rate, ~300 nl min^{-1}) into the mass spectrometer. The instrument was operated in a data-dependent mode cycling through a full scan (300–1,800 *m/z*, single µscan) followed by 10 HCD MS/MS scans on the 10 most abundant ions from the preceding full scan. The cations were isolated with a 2 Da mass window and set on a dynamic exclusion list for 60 s after they were first selected for MS/MS. The raw data were processed and analysed using MaxQuant (v.1.6.1.0). A fasta file containing yeast proteomes was downloaded from UniProt and used as protein sequence searching the database. Default parameters were adapted for the protein identification and quantification. Parent peak MS tolerance was 4.5 ppm, MS/MS tolerance was 20 ppm, the minimum peptide length was 7 amino acids, the maximum number of missed cleavages was 2. The proteins quantified were supported by at least two quantification events.

eSPAN method and data analysis

The eSPAN method was modified from previous studies with some modifications[32,33]. In brief, yeast G1 cells were released into a fresh medium containing BrdU, a thymidine analogue that can be incorporated into nascent DNA during DNA synthesis. The chromatin from early S phase cells was digested with micrococcal nuclease (MNase) and analysed using IP with antibodies against BrdU, followed by sequencing to identify DNA strands that contained BrdU (BrdU-IP-ssSeq). To identify nascent-DNA-associated nucleosomes, the MNase-digested chromatin was used for chromatin IP (ChIP) with antibodies against two different histone modifications: H3K56ac (a marker of newly formed histones) or H3K4me3 (a marker of parental histones), respectively. Subsequently, the chromatin immunoprecipitated DNA was denatured into single-stranded DNA and the newly synthesized DNA was enriched by BrdU IP, followed by strand-specific deep sequencing. The sequencing reads obtained from eSPAN were divided to distinguish between the Watson and Crick strands. The average ratio of Watson/Crick strands around early replication origins was then calculated. To minimize differences in BrdU incorporation, this ratio was normalized to the MNase-BrdU-IP-seq dataset. This calculation, known as eSPAN bias, provides information about the relative levels of a modified histone on the leading and lagging strands of DNA replication forks (Fig. 5a). To assess the efficiency of parental histone recycling on nascent strands, another ratio was calculated: the total eSPAN sequence reads surrounding the ACS (origin of replication) divided by the total MNase-BrdU-IP-seq reads in the same region. This measurement is referred to as eSPAN density. By separating eSPAN and BrdU-IP-seq sequence reads into Watson and Crick strands, the eSPAN density on nascent leading and lagging strand chromatin can be determined (Fig. 5a).

S. cerevisiae yeast cells were cultured in YPD medium at 30 °C to mid-log phase (OD_{600} = 0.45–0.5), and arrested at G1 phase by α-factor (5 mg ml^{-1}, 1000×, Chinese Peptide Company) at 25 °C. Cells were collected, washed with ice-cold double-distilled H_2O three times at 2,500 rpm for 5 min at 4 °C and then released into fresh YPD medium with 0.4 mg ml^{-1} BrdU (Sigma-Aldrich, B5002-5G) at 23 °C for 40 min to label nascent DNA. Cells were cross-linked with 1% (w/v) paraformaldehyde (Sigma-Aldrich, P6148-1KG) at 25 °C for 20 min and then quenched with 125 mM glycine (Amresco, 0167-5KG) at 25 °C for 5 min.

Cells (OD_{600} of around 100) were pelleted, and then washed twice with ice-cold 1× TBS buffer (0.1 mM PMSF freshly added) and then washed once with ice-cold buffer Z (1.2 M sorbitol, 50 mM Tris-HCl pH 7.4). The pellets were resuspended with 8.7 ml buffer Z (10 mM β-mercaptoethanol freshly added), and digested with 214 µl 5 mg ml^{-1} zymolase (Nacalai Tesque, 07665-84) at 28 °C for about 35 min to obtain spheroplasts. The efficiency of digestion was evaluated by measuring the OD_{600} in 1% SDS, with a decrease of over 90%. Pellets were collected, resuspended with 1.5 ml ice-cold NP buffer (1 M sorbitol, 50 mM NaCl, 10 mM Tris-HCl pH 7.4, 5 mM $MgCl_2$, 1 mM $CaCl_2$, with 0.5 mM spermidine, 0.007% (v/v) β-mercaptoethanol and 0.075% (v/v) NP-40 (Thermo Fisher Scientific, 28324) added freshly) and divided into four parts equally in LoBind tubes. For each part, a suitable amount of MNase (Worthington, LS004797) was added and incubated at 37 °C for about 20 min to digest the chromatin into mainly mono- and di-nucleosomes. Then, 8 µl 0.5 M EDTA (pH 8.0) was added to the reaction tube to stop the reaction. Next, 100 µl 5×ChIP lysis buffer (250 mM HEPES-KOH pH 7.5, 700 mM NaCl, 5 mM EDTA pH 8.0, 5% (v/v) Triton X-100, 0.5% (w/v) sodium deoxycholate, with 5 mM PMSF, 1.25 mg ml^{-1} pefabloc, 5 mg ml^{-1} bacitracin and 5 mM benzamidine

added freshly) was added, and the sample was then incubated for 30 min on ice. The lysate was then clarified by centrifugation twice at 10,800 rpm at 4 °C, with the first round lasting for 5 min and the second round lasting for 15 min. The supernatant was collected and ready for ChIP experiments.

For ChIP assays, 50 µl supernatant was taken as the input, and 800 µl supernatant was taken for ChIP using H3K4me3 (Abcam, ab8580) or H3K56ac[52] (prepared in-house) antibodies, with incubation at 4 °C for 12–16 h. The protein–DNA bound to antibodies was enriched using 20 µl prewashed protein G Sepharose agarose beads (GE Healthcare, 17061801) with 2 h of incubation at 4 °C. The binding system was then stepwise washed with the reagents below, and centrifuged at 2,500 rpm for 1 min at 4 °C: 1× ChIP lysis buffer (with 0.1 mM PMSF), once; 1× ChIP lysis buffer, incubated at 4 °C for 5 min, twice; 1× ChIP lysis buffer (with 0.5 M NaCl), once; 1× ChIP lysis buffer (with 0.5 M NaCl), incubated at 4 °C for 5 min, once; Tris/LiCl buffer, once; Tris/LiCl buffer, incubated at 4 °C for 5 min, once; Tris/EDTA buffer, twice. After washing, the liquid was removed using fine syringe needles. For both input and ChIP samples, 50 µl 20% (w/v) Chelex-100 (Bio-Rad, 1422822) was added, followed by boiling for 10 min at 100 °C for reverse-cross-linking. After cooling down, 5 µl of 20 mg ml^{-1} proteinase K (Invitrogen, 25530015) was added and the sample was incubated for 30 min at 55 °C. The sample was then boiled at 100 °C for another 10 min. The supernatant was saved after centrifuging at 14,000 rpm for 1 min, 75 µl for the input sample and 25 µl for the ChIP sample. Next, 50 µl 2× TE was added, followed by centrifuging at 14,000 rpm for 1 min. The 50 µl supernatant was saved and mixed with the previous one. For the ChIP sample, 35 µl 1×TE was also added, with 35 µl supernatant saved after centrifugation. For both input and ChIP samples, 90 µl of the total supernatant was taken for BrdU IP to get MNase-BrdU-IP and eSPAN samples, respectively.

For BrdU IP, the 90 µl sample was denatured by snap-cooling in an ice–water mixture for 5 min after 5 min of boiling at 100 °C. Then, 10 µl 10× PBS, 800 µl BrdU IP buffer (1× PBS, 0.0625% Triton X-100) with 0.3 µl *Escherichia coli* tRNA (Roche, 10109541001) and 0.36 µl anti-BrdU antibody (BD Biosciences, BD555627) were added into each sample, followed by 2 h of incubation at 4 °C. The BrdU-labelled nascent DNA bound to antibodies was then enriched using 15 µl prewashed protein G Sepharose agarose beads with another 2 h of incubation at 4 °C. The binding system was then washed with ice-cold BrdU IP buffer three times and with 1× TE once, with 4–5 min of incubation at 4 °C or room temperature, respectively. After washing, the remaining liquid was removed using fine syringe needles. Then, 100 µl elution buffer (1×TE, 1% (w/v) SDS) was added, and the sample was incubated at 65 °C for 15 min at 1,300 rpm on the Eppendorf Thermomixer C. Next, 85 µl supernatant was collected after centrifuging at 14,000 rpm for 1 min. Another 40 µl elution buffer was added, with incubation at 65 °C for 5 min at 1,300 rpm. Next, 35 µl supernatant was collected after centrifuging at 14,000 rpm for 1 min and mixed with the previous one. Together, six samples were generated: input, H3K4me3-ChIP, H3K56ac-ChIP, MNase-BrdU-IP, H3K4me3-eSPAN and H3K56ac-eSPAN. All of the samples were purified using the MinElute PCR Purification Kit (Qiagen) to prepare DNA for library construction. The quality of DNA was evaluated using quantitative PCR.

The single-stranded DNA libraries were constructed using the Accel-NGS 1S Plus DNA Library Kit for Illumina (Swift) and sequenced by the Novogene Genome Sequencing Company on the Illumina NovaSeq 6000 system. After quality control, the adapter and sequencing reads with low quality were removed using Trimmomatic[53]. Clean reads were mapped to the *S. cerevisiae* reference genome (sacCer3) using Bowtie2 (v.1.2.0)[54]. Only paired-end reads correctly mapped on both ends were selected for further analysis. On the basis of the flag in the SAM files, each read was assigned to the Watson or Crick strand using a custom Perl program. BrdU-enriched regions were called using MACS2[55]. DANPOS (v.2.2.2) was used to call nucleosome positions and occupancy[56]. The eSPAN bias was defined as the average log_2 ratio of the Watson strand reads over the Crick strand reads around 139 early DNA replication origins. To reduce the impact of the difference in the incorporation of BrdU among different strains, the eSPAN data were normalized to MNase-BrdU-IP-Seq data. The normalized eSPAN bias could represent the relative amount of histone modifications on the leading or lagging strand at the replication forks. The eSPAN density was calculated as the eSPAN signals at Watson or Crick strands around 139 early replication origins, after normalization to MNase-BrdU-IP-Seq data, which could measure the efficiency of parental histone recycling on leading or lagging strands. Statistical significance was tested using rank-sum Wilcoxon tests.

Reporting summary

Further information on research design is available in the Nature Portfolio Reporting Summary linked to this article.

Data availability

Coordinates and cryo-EM map data have been deposited at the Protein Data Bank and Electron Microscopy Data Bank under accession codes EMD-38317 and PDB 8XGC (composite map and the global atomic model), EMD-38316 (global structure, conformation-1), EMD-38314 (global structure, conformation-2), EMD-38313 (optimized local density map of Spt16-MD–histone) and EMD-38315 (optimized local density map of Polε). The raw sequencing data reported in this paper have been deposited in the Genome Sequence Archive at the National Genomics Data Center, Beijing Institute of Genomics (China National Center for Bioinformation), Chinese Academy of Sciences, under accession number GSA CRA012495. The data are publicly accessible online (https://bigd.big.ac.cn/gsa).

41. Zivanov, J. et al. New tools for automated high-resolution cryo-EM structure determination in RELION-3. *eLife* https://doi.org/10.7554/eLife.42166 (2018).
42. Zheng, S. Q. et al. MotionCor2: anisotropic correction of beam-induced motion for improved cryo-electron microscopy. *Nat. Methods* **14**, 331–332 (2017).
43. Rohou, A. & Grigorieff, N. CTFFIND4: Fast and accurate defocus estimation from electron micrographs. *J. Struct. Biol.* **192**, 216–221 (2015).
44. Bepler, T. et al. Positive-unlabeled convolutional neural networks for particle picking in cryo-electron micrographs. *Nat. Methods* **16**, 1153–1160 (2019).
45. Bepler, T., Kelley, K., Noble, A. J. & Berger, B. Topaz-Denoise: general deep denoising models for cryoEM and cryoET. *Nat. Commun.* **11**, 5208 (2020).
46. Adams, P. D. et al. PHENIX: a comprehensive Python-based system for macromolecular structure solution. *Acta Crystallogr. D* **66**, 213–221 (2010).
47. Pettersen, E. F. et al. UCSF Chimera—a visualization system for exploratory research and analysis. *J. Comput. Chem.* **25**, 1605–1612 (2004).
48. Pettersen, E. F. et al. UCSF ChimeraX: structure visualization for researchers, educators, and developers. *Protein Sci.* **30**, 70–82 (2021).
49. Jumper, J. et al. Highly accurate protein structure prediction with AlphaFold. *Nature* **596**, 583–589 (2021).
50. Emsley, P., Lohkamp, B., Scott, W. G. & Cowtan, K. Features and development of Coot. *Acta Crystallogr. D* **66**, 486–501 (2010).
51. Chen, V. B. et al. MolProbity: all-atom structure validation for macromolecular crystallography. *Acta Crystallogr. D* **66**, 12–21 (2010).
52. Li, Q. et al. Acetylation of histone H3 lysine 56 regulates replication-coupled nucleosome assembly. *Cell* **134**, 244–255 (2008).
53. Bolger, A. M., Lohse, M. & Usadel, B. Trimmomatic: a flexible trimmer for Illumina sequence data. *Bioinformatics* **30**, 2114–2120 (2014).
54. Langmead, B. & Salzberg, S. L. Fast gapped-read alignment with Bowtie 2. *Nat. Methods* **9**, 357–359 (2012).
55. Zhang, Y. et al. Model-based analysis of ChIP-seq (MACS). *Genome Biol.* **9**, R137 (2008).
56. Chen, K. et al. DANPOS: dynamic analysis of nucleosome position and occupancy by sequencing. *Genome Res.* **23**, 341–351 (2013).

Acknowledgements We thank K. Labib and T. Formosa for antibodies; and the members of the Biological Cryo-EM Center at the Hong Kong University of Science and Technology (HKUST) for data collection. The Cryo-EM Center at HKUST is supported by a donation from the Lo Kwee Seong Foundation. The computation was supported by the High-Performance Computing Platform of Peking University (PKU). We also thank the cryo-EM platform of PKU and the National Center for Protein Sciences at PKU for technical assistance. The work was supported by the National Natural Science Foundation of China (32321163647 to N.G., 31830048 to Q.L. and 31922036 to N.L.), the National Key R&D Program of China (2019YFA0508900 to Q.L. and 2019YFA0508904 to N.G.), the Beijing Outstanding Young Scientist Program (BJJWZYJH01201910001005) to Q.L., and the Research Grants Council (RGC) of Hong Kong (GRF17119022, GRF17109623, C7009-20GF, and CRS_HKU705/23 to Y. Zhai).

Author contributions Y. Zhai, N.G. and Q.L. conceived and supervised the project. Y.G., J. Li, Z.X. and Y. Zhai purified the replisome samples and conducted biochemical assays. J. Lin and X.D.L. performed quantitative MS analysis. D.Y. and Y.G. prepared cryo samples. D.Y., Yingyi Zhang and S.D. collected cryo-EM datasets. N.L. processed images. N.G., N.L. and Y. Zhai built atomic models. Yujie Zhang, J.F. and Q.L. performed eSPAN analyses. Y. Zhai, N.G., N.L., Y.G., Yujie Zhang, Q.L., J. Lin, X.D.L., B.K.T., Y.L. and K.Z. analysed the data, prepared the figures and wrote the manuscript.

Competing interests The authors declare no competing interests.

Additional information

Supplementary information The online version contains supplementary material available at https://doi.org/10.1038/s41586-024-07152-2.

Correspondence and requests for materials should be addressed to Bik Kwoon Tye, Qing Li, Ning Gao or Yuanliang Zhai.

Peer review information *Nature* thanks Hitoshi Kurumizaka and the other, anonymous, reviewer(s) for their contribution to the peer review of this work. Peer reviewer reports are available.

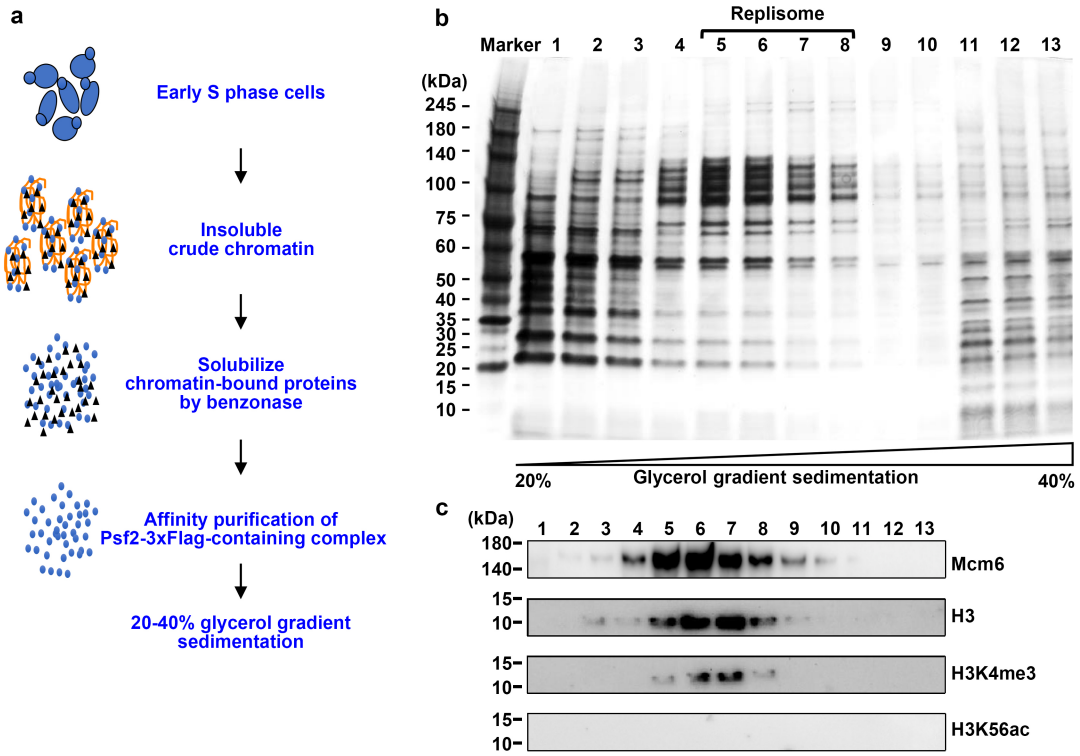

d

Protein name	riBAQ (10^{-3})
Psf3	97.2
Sld5	73.1
Hhf1	66.4
Psf2	59.5
Hta2	55.6
Ctf4	52.5
Mcm7	41.8
Mcm3	35.5
Mcm4	34.4
Cdc45	32.4
Psf1	31.8
Mcm5	30.8
Tof1	30.4
Mcm6	30.1
Mcm2	24.4
Dpb2	22.9
Pob3	21.5
Hht1	20.4
Spt16	19.2
Htb2	17.3
Dpb4	14.7
Mrc1	14.5
Pol2	13.9
Csm3	13.1
Top1	8.93
Pri2	3.16
Dpb3	2.74
Pol1	2.66
Pol12	2.18
Pri1	1.14

Extended Data Fig. 1 | Purification of the endogenous replisome. **a**, A flowchart of the procedures for replisome purification from early S chromatin of the yeast strain PSF2-3xFlag. **b-c**, SDS-PAGE analysis of the glycerol gradient (20-40%) fractions of the replisome sample eluted from anti-Flag affinity purification. The fractions were resolved and visualized by silver staining (**b**) and immunoblotting of the proteins as indicated (**c**). Fractions 5-8 containing replisome-FACT-histones were pooled and processed for mass spectrometry analysis. Based on this result, similar fractions containing crosslinked samples after grafix were pooled and processed for further EM analyses. Similar results were obtained at least in two independent experiments. **d**, The major proteins associated with the endogenous replisome identified by quantitative liquid chromatography mass spectrometry (LC-MS). For gel source data, see Supplementary Fig. 1.

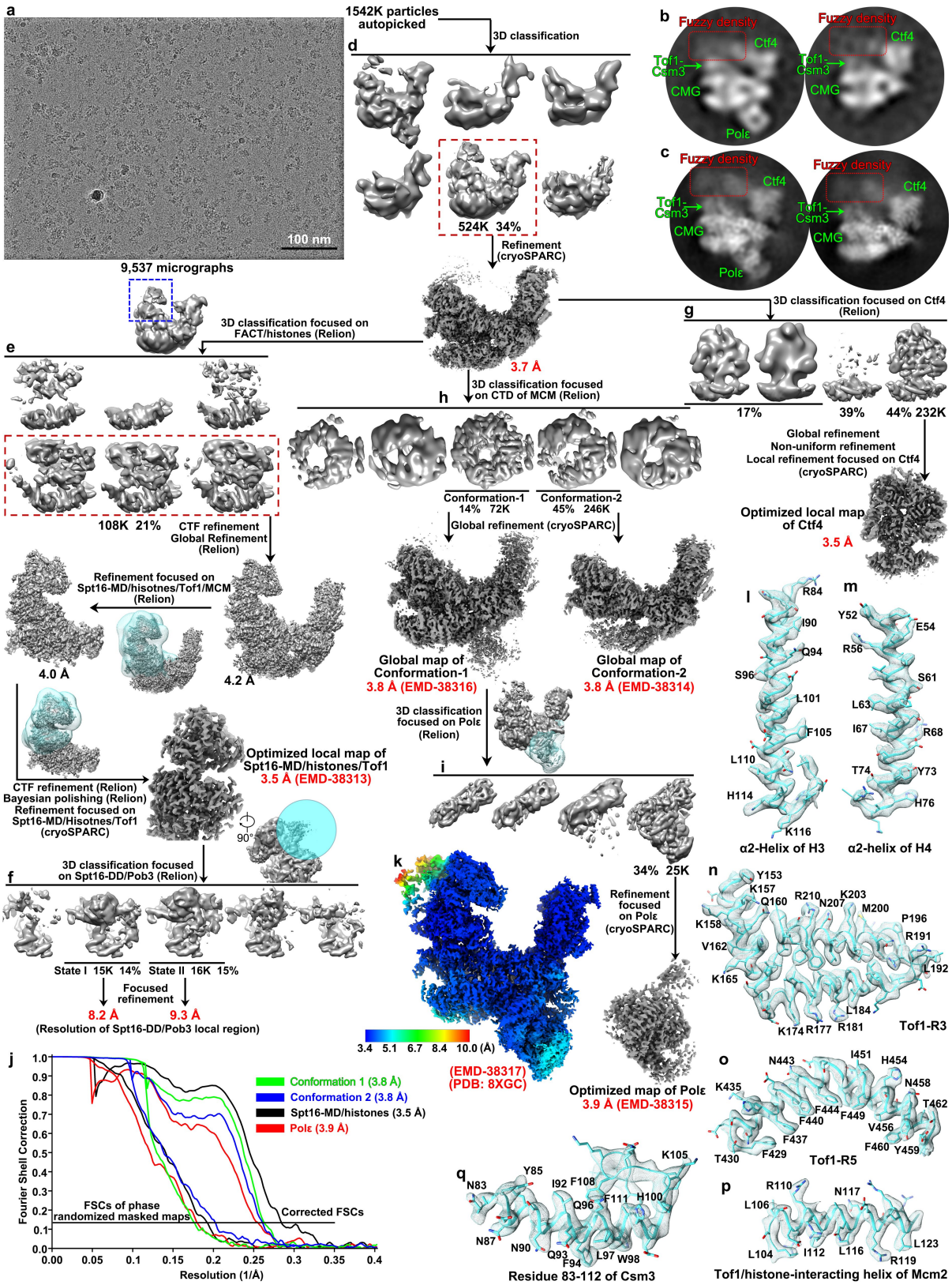

Extended Data Fig. 2 | Cryo-EM image processing of the replisome sample. **a**, A representative raw cryo-EM image of the replisome sample. **b-c**, 2D class averages of negative staining (**b**) and cryo-EM (**c**) replisome particles. **d-i**, Workflow of image processing of the replisome cryo-EM images. See Methods for details. **j**, Corrected (the right line group) and phase randomized (the left line group) FSC curves of the final global and local density maps for the replisome complex. **k**, The local resolutions of the composite replisome map were colour coded. **l-q**, Cryo-EM densities for indicated regions of the replisome.

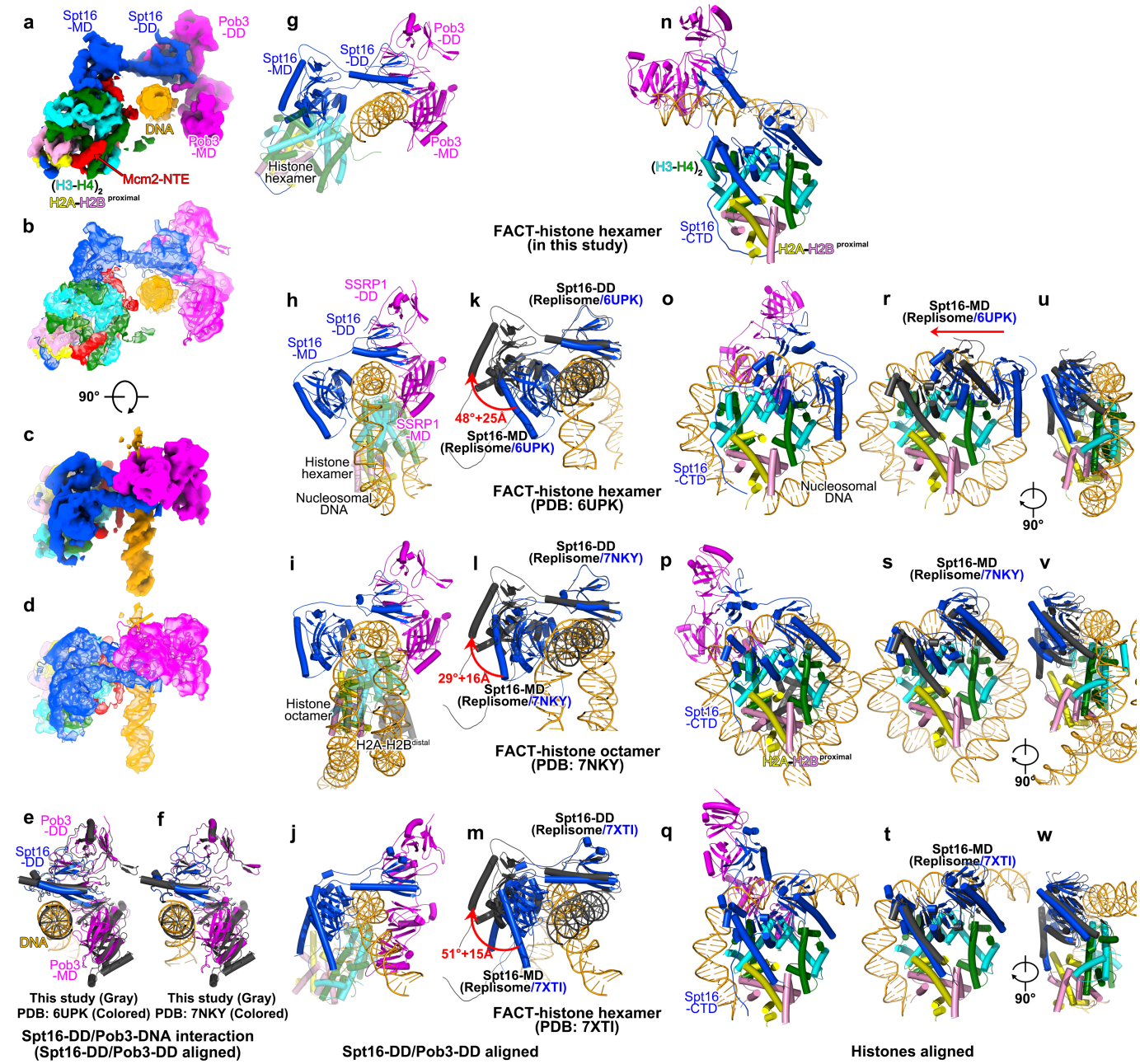

Extended Data Fig. 3 | Conformational change in FACT during substrate transaction. a, **c**, Different views of the local density map of the FACT-histones complex bound with parental duplex DNA. **b**, **d**, same as (**a**, **c**) respectively but superimposed with the atomic model. **e**-**f**, FACT-DNA interaction. Comparison of the Spt16-DD/Pob3-DD-DNA structure from the replisome (this study) with those from FACT-hexasome (PDB: 6UPK) (**e**) and RNA Polymerase II-Spt4/5-nucleosome-FACT (PDB: 7NKY) (**f**). Spt16-DD/Pob3-DD was used as a reference for alignment. **g**-**j**, Comparison of the FACT structures from the replisome-histone hexamer-FACT (this study) (**g**), human FACT-hexasome (PDB: 6UPK) (**i**), yeast RNA Polymerase II-Spt4/5-nucleosome-FACT (PDB: 7NKY) (**j**), and RNA polymerase II elongation complex-nucleosome-FACT (*Komagataella phaffii*) (EC58hex, PDB: 7XTI) (**j**). Spt16-DD/Pob3-DD was used as a reference for alignment. **k**-**m**, Superimposition of the FACT structure from the replisome (this study, **g**) with those from **h**-**j** to highlight the conformational changes in Spt16 bound with different substrates as indicated, respectively. Spt16-DD/Pob3-DD was used as a reference for alignment. **n**-**w**, The relevant structures from **g**-**m** were aligned using histones as a reference to illustrate the conformational changes in both Spt16 and Pob3 while relocating histones onto Tof1 at replication fork during parental histone recycling. The histones and DNA from the replisome were omitted to highlight the movement of Spt16-MD in **r**-**w**.

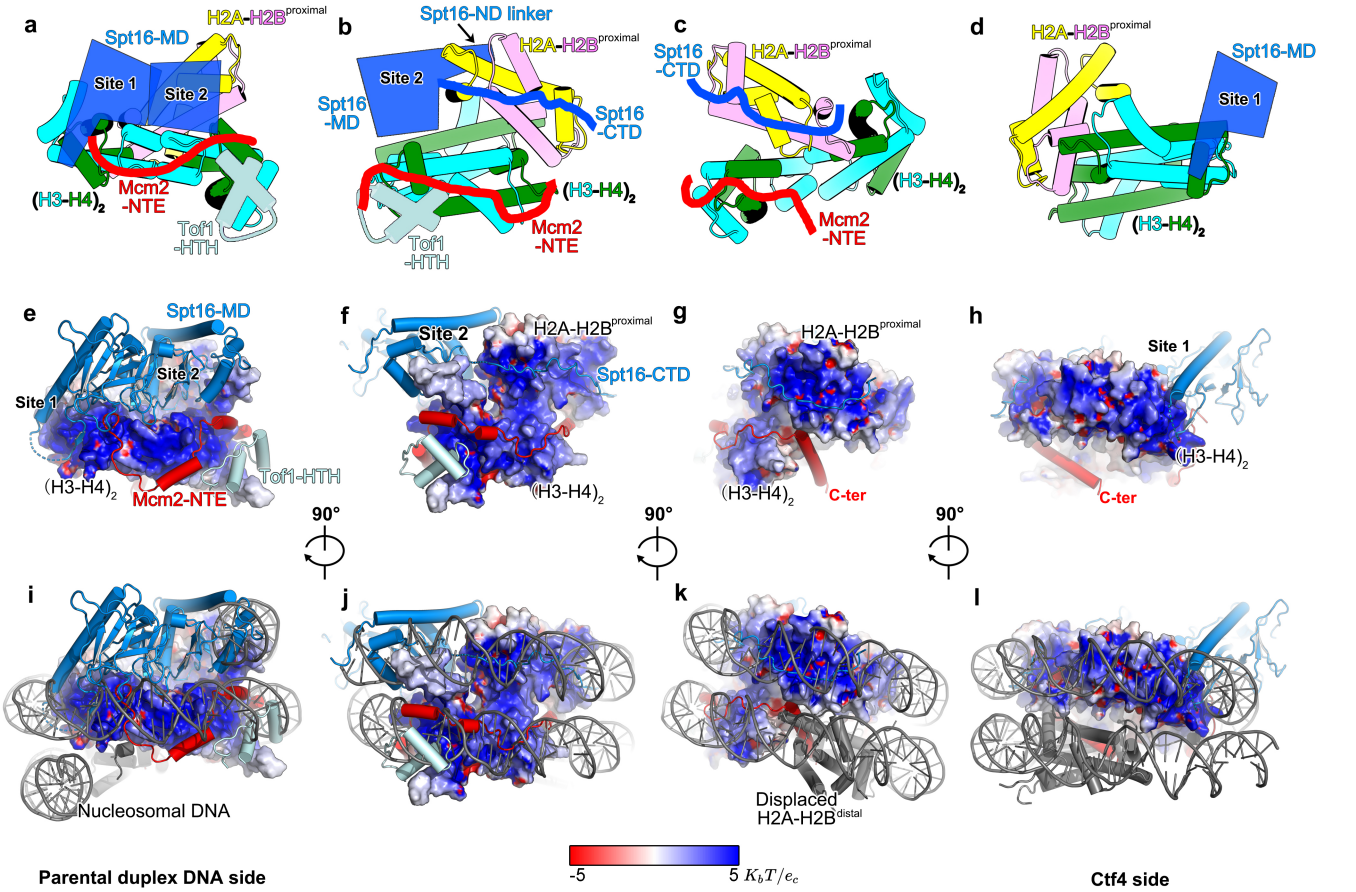

Extended Data Fig. 4 | The histone hexamer is shielded by its chaperones at the replication fork. a-d, Schematic illustration of the histone-chaperone interaction in the replisome. **e-f**, Side views of the electrostatic surfaces of the histone hexamer highlighting its associations with Spt16-MD, Mcm2-NTE, and Tof1-HTH for shielding its DNA binding surfaces. **i-l**, same as (**e-f**) but superimposed with the nucleosomal DNA from an intact nucleosome (PDB: 1ID3).

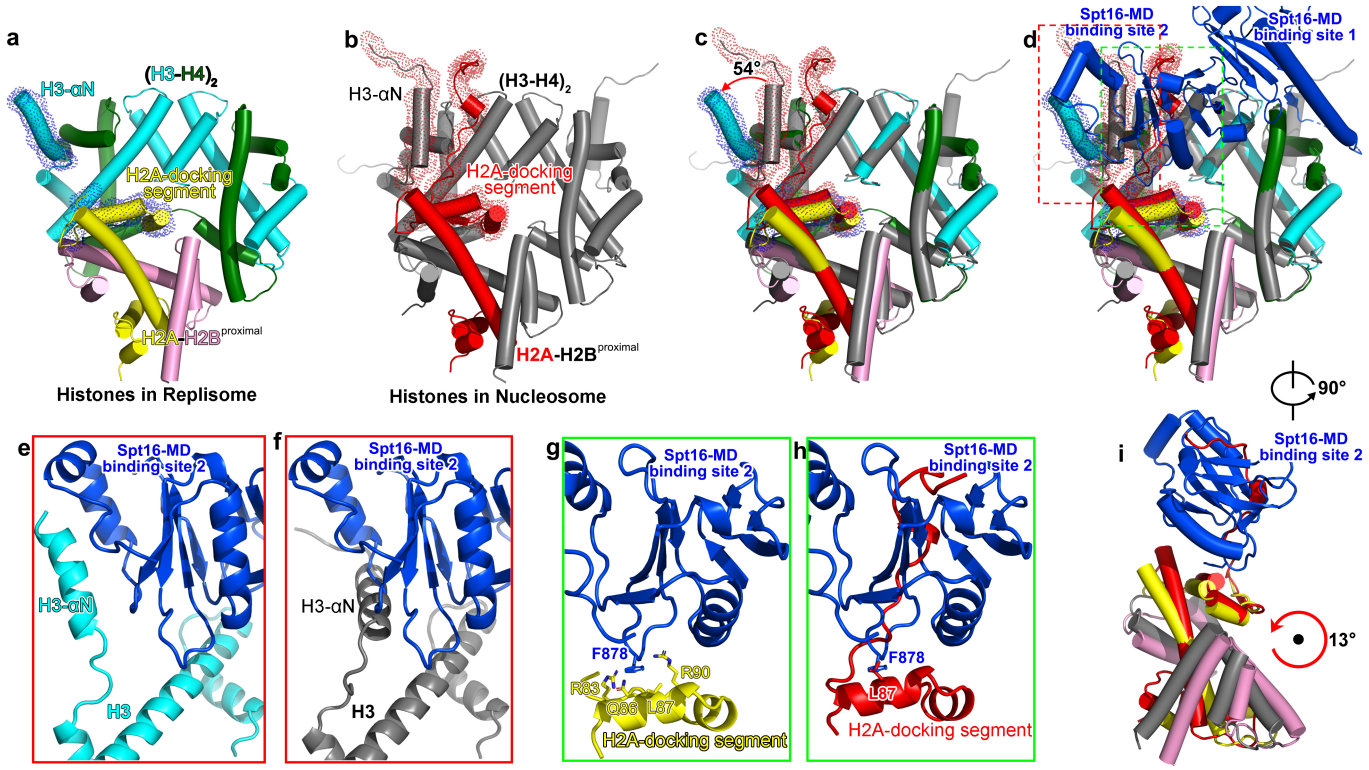

Extended Data Fig. 5 | Small displacement of H2A-H2B^{proximal} by Spt16-MD. **a-c**, Comparison of the histone structures from the replisome (**a**) and an intact nucleosome (PDB: 1ID3) (**b**). Superimposition of these two structures using $(H3\text{-}H4)_2$ as a reference for alignment (**c**). H3-αN and H2A-docking segment were coated with transparent surface presentation to highlight conformational changes occurring upon these regions in the replisome. **d**, Same as (**c**) but with Spt16-MD from the replisome visible to illustrate the steric conflict between Spt16-MD and H3-αN/H2A-docking segment on H3-H4 tetramer. **e**, Zoomed-in view of the boxed region (red box) in (**d**) but with the region from the replisome shown only. **f**, Same as (**e**) but shown with the H3 from the intact nucleosome (grey) and with Spt16-MD from the replisome superimposed. **g**, Zoomed-in view of the boxed region (green box) in (**d**) but with the region from the replisome shown only. The key residues involved in the interaction between Spt16-MD and H2A-docking segment are shown in stick and labelled. **h**, Same as (**g**) but shown with the H2A-docking segment from the intact nucleosome (red) and with Spt16-MD from the replisome superimposed. **i**, Same as (**d**) but with a 90°-rotation. The $(H3\text{-}H4)_2$ tetramer is not shown to highlight a 13°-rotation in the H2A-H2B^{proximal} upon Spt16-MD binding.

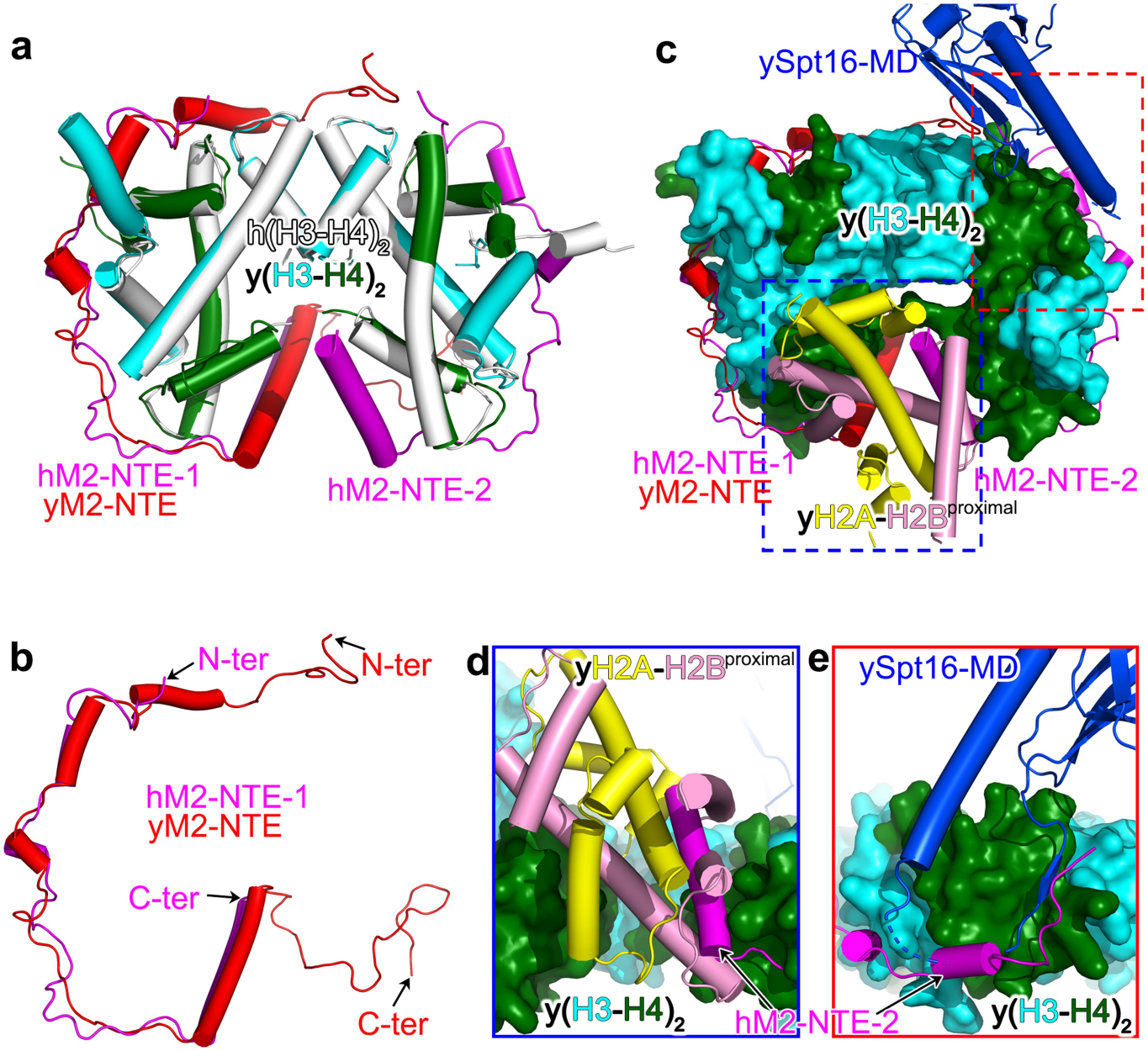

Extended Data Fig. 6 | The arrangement of Mcm2-NTE around the evicted histones is pre-determined by Spt16-MD and H2A-H2B^{proximal}. a, Structural comparison of the $(H3\text{-}H4)_2$/MCM2-NTE interactions from the structures of human $(H3\text{-}H4)_2$-MCM2-HBD (PDB:5BNV) and yeast histone hexamer-Mcm2-NTE-Spt16-MD from the replisome (this study). H3-H4 was used as a reference for alignment. h: human; y: yeast; M2: MCM2. **b**, Same as (**a**) but with hM2-NTE-1 and yM2-NTE shown only. **c**, Same as (**a**) but with $y(H3\text{-}H4)_2$ shown in surface presentation and other subunits and motifs in cartoon presentation. **d-e**, Zoomed-in views of the boxed regions in (**c**).

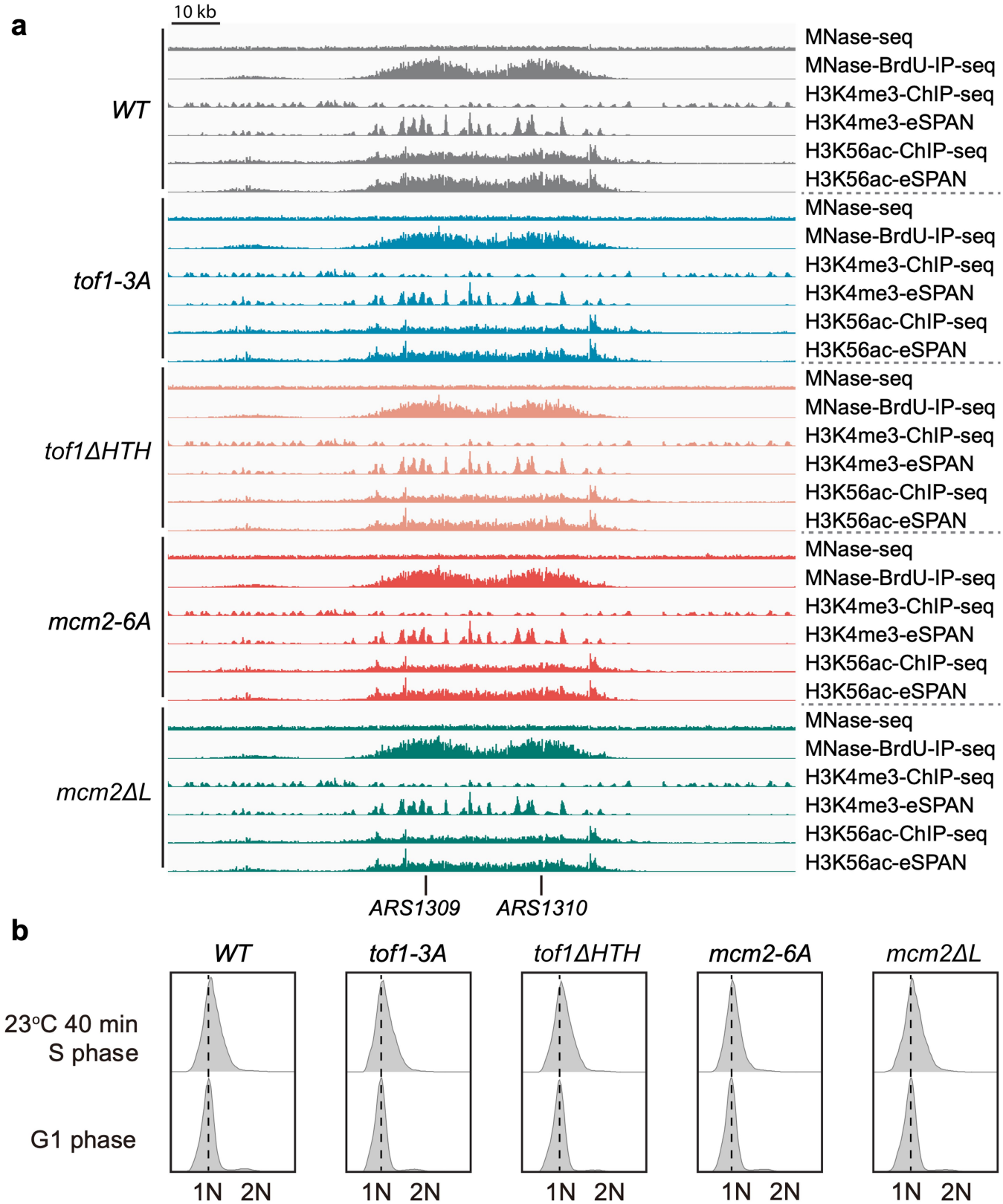

Extended Data Fig. 7 | eSPAN analysis of the interaction between Tof1 and Mcm2. a, Snapshot of MNase-seq, MNase-BrdU-IP-seq, H3K4me3-ChIP-seq, H3K4me3-eSPAN, H3K56ac-ChIP-seq, and H3K56ac-eSPAN datasets around replication origins ARS1309 and ARS1310 in wild-type (WT), *tof1-3A*, *tof1ΔHTH*, *mcm2-6A*, and *mcm2ΔL*. The scale bar represents a 10-kilo base pair (kbp) DNA region. **b**, DNA content analysis of the eSPAN samples. Cellular DNA content was measured by flow cytometry with PI staining. Similar results were obtained in two independent experiments. See Methods for more details.

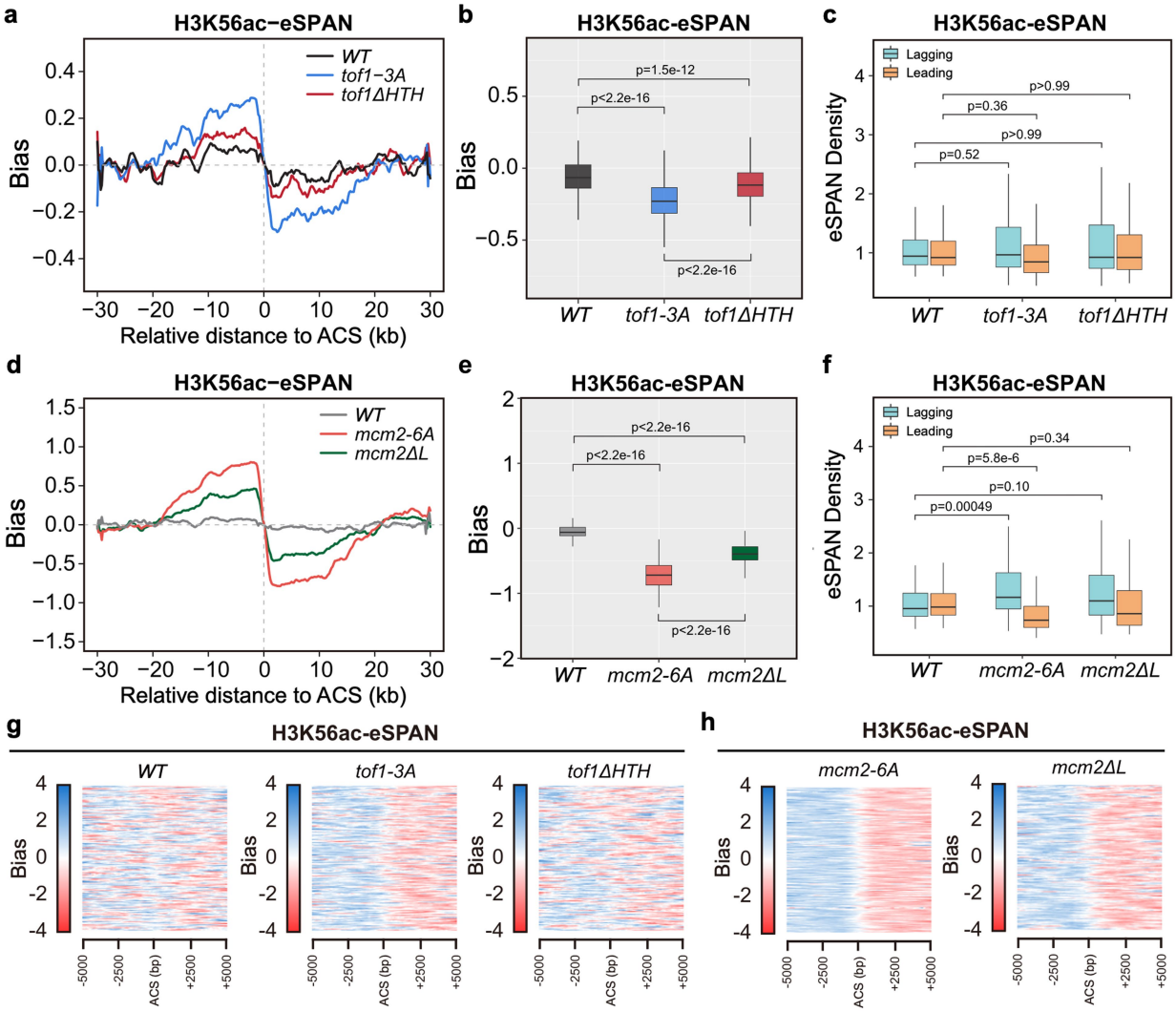

Extended Data Fig. 8 | The interaction between Tof1 and Mcm2 affects the relative amounts of the newly synthesized histone deposition between the leading and lagging strands. a, Line plots of the H3K56ac eSPAN bias show the relative amount of new histone deposition between the two daughter strands in wild-type (WT), *tof1-3A*, and *tof1ΔHTH* cells. The H3K56ac-eSPAN bias around 139 early replication origins of the autonomous replication sequences (ACSs) was calculated. **b**, Box plots of the H3K56ac-eSPAN bias around the 139 ACSs in WT, *tof1-3A*, and *tof1ΔHTH* mutant cells are shown ($n = 139$). **c**, Box plots showing the H3K56ac-eSPAN density on both leading and lagging strands in WT, *tof1-3A*, and *tof1ΔHTH* cells ($n = 139$). **d**, Line plots of the H3K56ac eSPAN bias around the 139 ACSs in wild-type (WT), *mcm2-6A*, and *mcm2ΔL* cells are shown. **e**, Box plots of the H3K56ac-eSPAN bias around the 139 ACSs in WT and *mcm2-6A* or *mcm2ΔL* mutant cells are shown ($n = 139$). **f**, Box plots showing the H3K56ac-eSPAN density on both leading and lagging strands in WT, *mcm2-6A*, and *mcm2ΔL* cells ($n = 139$). **g-h**, Heatmap analysis of the H3K56ac-eSPAN bias around 139 ACSs in WT, *tof1-3A*, *tof1ΔHTH* (**g**), *mcm2-6A*, and *mcm2ΔL* (**h**) cells. Box plots (**b, c, e, f**) show the median, minimal, maximal, and 25% and 75% quartiles values. *P* values calculated using two-sided rank-sum Wilcoxon test. Similar results were obtained in two independent experiments. See Methods for more details.

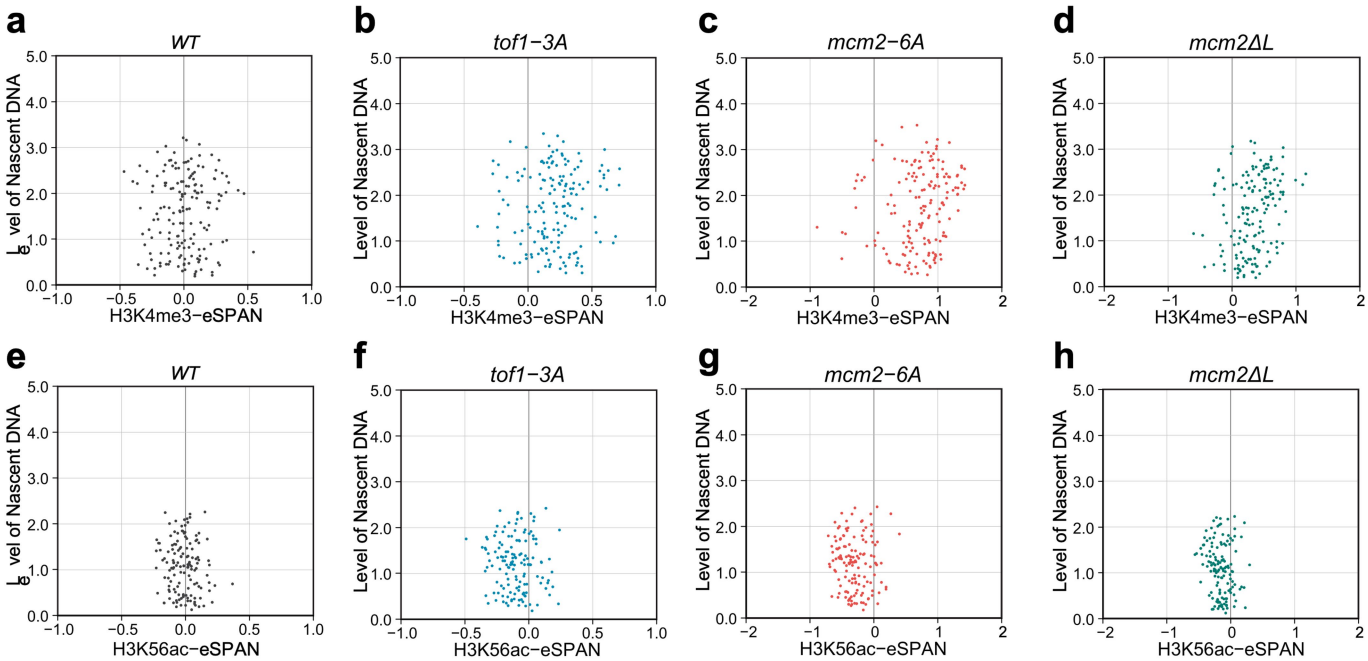

Extended Data Fig. 9 | The asymmetric histone partitioning between daughter strands in the disrupted Tof1-Mcm2 interaction cells does not result from defects in DNA replication. a-d, The statistical results of correlation between BrdU incorporation level and H3K4me3-eSPAN value at each ACS region in *WT* (a), *tof1-3A* (b), *mcm2-6A* (c) and *mcm2ΔL* (d) cells. Dot scatterplot showing the distribution of the H3K4me3-eSPAN bias at early replication origins ($n = 139$). **e-h**, The statistical results of correlation between BrdU incorporation level and H3K56ac-eSPAN value at each ACS region in *WT* (e), *tof1-3A* (f), *mcm2-6A* (g) and *mcm2ΔL* (h) cells. Dot scatterplot showing the distribution of the H3K56ac-eSPAN bias at early replication origins ($n = 139$). Similar results were obtained in two independent experiments.

Extended Data Table 1 | Cryo-EM data collection, refinement, and validation statistics

	Composite map (EMDB-38317) (PDB 8XGC)	Global map (Conformation-1) (EMDB-38316)	Global map (Conformation-2) (EMDB-38314)	Local map of Spt16/histones (EMDB-38313)	Local map of Polε (EMDB-38315)
Data collection and processing					
Electron micrograph	FEI Titan Krios G3i TEM				
Camera	Gatan GIF K3				
Magnification	81,000x				
Voltage (kV)	300				
Electron exposure ($e^-/Å^2$)	50				
Total frames	40				
Dose rate ($e^-/Å^2/s$)	12.5				
Defocus range (μm)	-1.0 to -2.5				
Pixel size (Å)	1.06				
Symmetry imposed	C1				
Initial particle images (no.)	1542K				
Final particle images (no.)	n/a	72K	246K	108K	25K
Map resolution (Å)	3.7	3.8	3.8	3.5	3.9
FSC threshold	0.143				
Map resolution range (Å)	3.4-16.1	3.5-20.3	3.5-17.3	3.3-8.9	3.8-10.6
Refinement					
Initial model used (PDB code)	1ID3, 5BNV, 6SKL, 7NKY				
Model resolution (Å)	3.7				
FSC threshold	0.143				
Model resolution range (Å)	3.6-16.1				
Map sharpening *B* factor ($Å^2$)	n/a	116	n/a	50	100
Model composition					
Non-hydrogen atoms	82765				
Protein residues	10319				
Nucleotides	90				
Ligands (Zn^{2+})	7				
Ligands (ADP)	5				
B factors ($Å^2$)					
Protein	72				
Ligand	87				
R.m.s. deviations					
Bond lengths (Å)	0.0045				
Bond angles (°)	0.93				
Validation					
MolProbity score	1.45				
Clashscore	5.28				
Poor rotamers (%)	0.02				
Ramachandran plot					
Favored (%)	97.06				
Allowed (%)	2.94				
Disallowed (%)	0.00				

nature portfolio

Corresponding author(s): Bik Tye
Qing Li,
NIng Gao,
Yuanliang Zhai

Last updated by author(s): Jan 9, 2024

Reporting Summary

Nature Portfolio wishes to improve the reproducibility of the work that we publish. This form provides structure for consistency and transparency in reporting. For further information on Nature Portfolio policies, see our Editorial Policies and the Editorial Policy Checklist.

Statistics

For all statistical analyses, confirm that the following items are present in the figure legend, table legend, main text, or Methods section.

n/a	Confirmed	
☐	☒	The exact sample size (*n*) for each experimental group/condition, given as a discrete number and unit of measurement
☐	☒	A statement on whether measurements were taken from distinct samples or whether the same sample was measured repeatedly
☐	☒	The statistical test(s) used AND whether they are one- or two-sided *Only common tests should be described solely by name; describe more complex techniques in the Methods section.*
☒	☐	A description of all covariates tested
☐	☒	A description of any assumptions or corrections, such as tests of normality and adjustment for multiple comparisons
☐	☒	A full description of the statistical parameters including central tendency (e.g. means) or other basic estimates (e.g. regression coefficient) AND variation (e.g. standard deviation) or associated estimates of uncertainty (e.g. confidence intervals)
☐	☒	For null hypothesis testing, the test statistic (e.g. *F*, *t*, *r*) with confidence intervals, effect sizes, degrees of freedom and *P* value noted *Give P values as exact values whenever suitable.*
☒	☐	For Bayesian analysis, information on the choice of priors and Markov chain Monte Carlo settings
☒	☐	For hierarchical and complex designs, identification of the appropriate level for tests and full reporting of outcomes
☐	☒	Estimates of effect sizes (e.g. Cohen's *d*, Pearson's *r*), indicating how they were calculated

Our web collection on statistics for biologists contains articles on many of the points above.

Software and code

Policy information about availability of computer code

Data collection	EPU-v2.12, Illumina NovaSeq6000
Data analysis	MotionCor2-v1.4.0, CTFFIND4-v4.1.13, RELION-v4.0, CryoSPARC-v4.0, Topaz-v0.2.5, PyMol-v2.5.2, UCSF Chimera-v1.11.2, UCSF ChimeraX-v1.3, Coot-v0.9.8.92, Phenix-v1.19.2, Trimmomatic, Bowtie 2-v1.2.0, MACS2, DANPOS-v2.2.2

For manuscripts utilizing custom algorithms or software that are central to the research but not yet described in published literature, software must be made available to editors and reviewers. We strongly encourage code deposition in a community repository (e.g. GitHub). See the Nature Portfolio guidelines for submitting code & software for further information.

Data

Policy information about availability of data

All manuscripts must include a data availability statement. This statement should provide the following information, where applicable:

- Accession codes, unique identifiers, or web links for publicly available datasets
- A description of any restrictions on data availability
- For clinical datasets or third party data, please ensure that the statement adheres to our policy

Coordinates and cryo-EM map have been deposited in the Protein Data Bank and EM databank with accession code: EMD-38317, PDB: 8XGC (Composite map and the global atomic model), EMD-38316 (Global structure, Conformation-1), EMD-38314 (Global structure, Conformation-2), EMD-38313 (Optimized local density map of Spt16-MD/histones), and EMD-38315 (Optimized local density map of Pol epsilon), respectively.

The raw sequence data reported in this paper have been deposited in the Genome Sequence Archive at the National Genomics Data Center, Beijing Institute of Genomics (China National Center for Bioinformation), Chinese Academy of Sciences, under accession number(s) GSA: CRA012495. The data are publicly accessible at https://bigd.big.ac.cn/gsa.

Research involving human participants, their data, or biological material

Policy information about studies with human participants or human data. See also policy information about sex, gender (identity/presentation), and sexual orientation and race, ethnicity and racism.

Reporting on sex and gender	N/A
Reporting on race, ethnicity, or other socially relevant groupings	N/A
Population characteristics	N/A
Recruitment	N/A
Ethics oversight	N/A

Note that full information on the approval of the study protocol must also be provided in the manuscript.

Field-specific reporting

Please select the one below that is the best fit for your research. If you are not sure, read the appropriate sections before making your selection.

☒ Life sciences ☐ Behavioural & social sciences ☐ Ecological, evolutionary & environmental sciences

For a reference copy of the document with all sections, see nature.com/documents/nr-reporting-summary-flat.pdf

Life sciences study design

All studies must disclose on these points even when the disclosure is negative.

Sample size	No statistical methods were used to determined sample size. Sample size was chosen empirically through laboratory experience (PMID: 3773068; PMID: 35296675; PMID: 29973722; PMID: 26222030). For biochemical experiments, including protein purification, glycerol gradient sedimentation and SDS-PAGE were done in biological replicates (N=2 to 4) and showed to have excellent reproducibility.
Data exclusions	Regarding the cryo-EM raw micrograph screening, exclusion was done based on the quality of the images. Regarding the particle selection, 2D and 3D classification were used and criterion is based on the quality of resulting 2D class average and 3D maps.
Replication	All data was replicated at least twice in independent studies. All attempts of replication was successful.
Randomization	Samples were not allocated to groups.
Blinding	Investigators were not blinded during data acquisition and analysis because because visual inspection is necessary for the methods employed.

Reporting for specific materials, systems and methods

We require information from authors about some types of materials, experimental systems and methods used in many studies. Here, indicate whether each material, system or method listed is relevant to your study. If you are not sure if a list item applies to your research, read the appropriate section before selecting a response.

Materials & experimental systems

n/a	Involved in the study
☐	☒ Antibodies
☐	☒ Eukaryotic cell lines
☒	☐ Palaeontology and archaeology
☒	☐ Animals and other organisms
☒	☐ Clinical data
☒	☐ Dual use research of concern
☒	☐ Plants

Methods

n/a	Involved in the study
☐	☒ ChIP-seq
☐	☒ Flow cytometry
☒	☐ MRI-based neuroimaging

Antibodies

Antibodies used	MCM6 (a gift from Karim Labib, 1;20,000), histone H3 (Abcam, ab1791, 1:2,500), H3K4me3 (Abcam, ab8580, 1:1,000), H3K56Ac (homemade by Qing Li's lab, 1:1,000) PMID: 18662540, BrdU antibody (BD Biosciences, BD555627)
Validation	All antibodies used in this study have been validated by the manufacturer and previous publications. Anti-MCM6 antibody (a gift from Karim Labib, School of Life Sciences, University of Dundee) was raised in sheep. Western blot was also done to validate the specificity of antibodies towards Mcm6 (PMID: 16531994). Anti-H3 (Abcam, ab1791) has been validated the vendor: https://www.abcam.com/products/primary-antibodies/histone-h3-antibody-nuclear-marker-and-chip-grade-ab1791.html Anti-H3K4me3 (Abcam, ab8580) has been validated by the vendor: https://www.abcam.cn/products/primary-antibodies/histone-h3-tri-methyl-k4-antibody-chip-grade-ab8580.html Antiserum against H3 acetylated at lysine 56 (H3K56Ac) was generated in rabbit, and H3K56Ac-specific antibodies were affinity purified and validated in our previous publication (PMID: 18662540).

Eukaryotic cell lines

Policy information about cell lines and Sex and Gender in Research

Cell line source(s)	Yeast W303-1a
Authentication	The cell lines were used only for protein purification and functional analyses, and not further authenticated.
Mycoplasma contamination	The cell lines used in this study were not tested for this contamination.
Commonly misidentified lines (See ICLAC register)	No cell line used in this study was commonly misidentified lines.

Plants

Seed stocks	N/A
Novel plant genotypes	N/A
Authentication	N/A

ChIP-seq

Data deposition

☒ Confirm that both raw and final processed data have been deposited in a public database such as GEO.

☒ Confirm that you have deposited or provided access to graph files (e.g. BED files) for the called peaks.

Data access links *May remain private before publication.*	The reviewer link is: https://ngdc.cncb.ac.cn/gsa/s/wdcB8CTQ GSA: CRA012495
Files in database submission	i5_1.fq.gz i5_2.fq.gz B5_1.fq.gz B5_2.fq.gz Cm5_1.fq.gz Cm5_2.fq.gz Ca5_1.fq.gz Ca5_2.fq.gz Em5_1.fq.gz Em5_2.fq.gz Ea5_1.fq.gz Ea5_2.fq.gz i9_1.fq.gz i9_2.fq.gz B9_1.fq.gz B9_2.fq.gz Cm9_1.fq.gz Cm9_2.fq.gz Ca9_1.fq.gz Ca9_2.fq.gz Em9_1.fq.gz

Em9_2.fq.gz
Ea9_1.fq.gz
Ea9_2.fq.gz
it16_1.fq.gz
it16_2.fq.gz
Bt16_1.fq.gz
Bt16_2.fq.gz
Cmt16_1.fq.gz
Cmt16_2.fq.gz
Cat16_1.fq.gz
Cat16_2.fq.gz
Emt16_1.fq.gz
Emt16_2.fq.gz
Eat16_1.fq.gz
Eat16_2.fq.gz
it21_1.fq.gz
it21_2.fq.gz
Bt21_1.fq.gz
Bt21_2.fq.gz
Cmt21_1.fq.gz
Cmt21_2.fq.gz
Cat21_1.fq.gz
Cat21_2.fq.gz
Emt21_1.fq.gz
Emt21_2.fq.gz
Eat21_1.fq.gz
Eat21_2.fq.gz
it15_1.fq.gz
it15_2.fq.gz
Bt15_1.fq.gz
Bt15_2.fq.gz
Cmt15_1.fq.gz
Cmt15_2.fq.gz
Cat15_1.fq.gz
Cat15_2.fq.gz
Emt15_1.fq.gz
Emt15_2.fq.gz
Eat15_1.fq.gz
Eat15_2.fq.gz
it17_1.fq.gz
it17_2.fq.gz
Bt17_1.fq.gz
Bt17_2.fq.gz
Cmt17_1.fq.gz
Cmt17_2.fq.gz
Cat17_1.fq.gz
Cat17_2.fq.gz
Emt17_1.fq.gz
Emt17_2.fq.gz
Eat17_1.fq.gz
Eat17_2.fq.gz
it18_1.fq.gz
it18_2.fq.gz
Bt18_1.fq.gz
Bt18_2.fq.gz
Cmt18_1.fq.gz
Cmt18_2.fq.gz
Cat18_1.fq.gz
Cat18_2.fq.gz
Emt18_1.fq.gz
Emt18_2.fq.gz
Eat18_1.fq.gz
Eat18_2.fq.gz
it22_1.fq.gz
it22_2.fq.gz
Bt22_1.fq.gz
Bt22_2.fq.gz
Cmt22_1.fq.gz
Cmt22_2.fq.gz
Cat22_1.fq.gz
Cat22_2.fq.gz
Emt22_1.fq.gz
Emt22_2.fq.gz
Eat22_1.fq.gz
Eat22_2.fq.gz
it19_1.fq.gz

it19_2.fq.gz
Bt19_1.fq.gz
Bt19_2.fq.gz
Cmt19_1.fq.gz
Cmt19_2.fq.gz
Cat19_1.fq.gz
Cat19_2.fq.gz
Emt19_1.fq.gz
Emt19_2.fq.gz
Eat19_1.fq.gz
Eat19_2.fq.gz
it23_1.fq.gz
it23_2.fq.gz
Bt23_1.fq.gz
Bt23_2.fq.gz
Cmt23_1.fq.gz
Cmt23_2.fq.gz
Cat23_1.fq.gz
Cat23_2.fq.gz
Emt23_1.fq.gz
Emt23_2.fq.gz
Eat23_1.fq.gz
Eat23_2.fq.gz

Genome browser session (e.g. UCSC)

No longer applicable.

Methodology

Replicates

2 for all experiments

Sequencing depth

All samples were sequenced as pair-end, 150 nt reads.

sample | Total reads (M) | Alignment rate
i5 | 7.93 | 93.8%
B5 | 6.80 | 95.2%
Cm5 | 11.9 | 92.9%
Ca5 | 7.99 | 93.6%
Em5 | 15.1 | 93.2%
Ea5 | 17.8 | 94.2%
i9 | 7.92 | 93.7%
B9 | 13.1 | 94.8%
Cm9 | 8.57 | 93.8%
Ca9 | 12.0 | 92.7%
Em9 | 16.1 | 92.6%
Ea9 | 12.5 | 92.6%
it16 | 6.50 | 95.4%
Bt16 | 8.58 | 96.9%
Cmt16 | 9.05 | 94.6%
Cat16 | 5.04 | 96.4%
Emt16 | 10.0 | 96.0%
Eat16 | 12.7 | 96.0%
it21 | 4.85 | 95.6%
Bt21 | 4.52 | 97.2%
Cmt21 | 13.0 | 95.6%
Cat21 | 17.2 | 95.1%
Emt21 | 13.1 | 89.2%
Eat21 | 19.4 | 93.1%
it15 | 5.01 | 95.4%
Bt15 | 5.62 | 97.3%
Cmt15 | 14.2 | 95.1%
Cat15 | 12.8 | 96.2%
Emt15 | 18.6 | 95.6%
Eat15 | 7.92 | 97.0%
it17 | 7.13 | 93.8%
Bt17 | 5.73 | 96.3%
Cmt17 | 14.7 | 94.4%
Cat17 | 14.6 | 96.0%
Emt17 | 13.2 | 93.7%
Eat17 | 12.6 | 94.0%
it18 | 7.46 | 94.8%
Bt18 | 6.07 | 96.9%
Cmt18 | 9.18 | 95.3%
Cat18 | 17.2 | 96.2%
Emt18 | 10.6 | 93.6%
Eat18 | 15.8 | 94.7%

it22 | 4.40 | 96.0%
Bt22 | 7.24 | 97.2%
Cmt22 | 11.0 | 95.9%
Cat22 | 20.4 | 95.0%
Emt22 | 11.2 | 88.2%
Eat22 | 16.4 | 92.6%
it19 | 8.23 | 95.2%
Bt19 | 5.90 | 97.0%
Cmt19 | 16.3 | 94.0%
Cat19 | 13.3 | 96.3%
Emt19 | 16.2 | 94.3%
Eat19 | 13.4 | 95.4%
it23 | 6.65 | 96.0%
Bt23 | 6.40 | 97.3%
Cmt23 | 16.5 | 95.4%
Cat23 | 11.9 | 94.0%
Emt23 | 15.3 | 92.4%
Eat23 | 10.9 | 93.9%

Antibodies

H3K4me3: Abcam ab8580, see above for validation
H3K56ac: developed in-house, see above for validation

Peak calling parameters

Peaks were called using MACS2 with --nomodel --broad.

Data quality

Sequences with low quality score were removed with Trimmomatic. Only paired-end reads correctly mapped on both ends were selected for further analysis. Replicated were examined to ensure reproducibility.

Numbers of peaks FDR<5%
B5w 911
B5c 1091
B9w 1083
B9c 1311
Bt16w 1382
Bt16c 1548
Bt21w 1547
Bt21c 1572
Bt15w 1252
Bt15c 1362
Bt17w 1507
Bt17c 1519
Bt18w 1379
Bt18c 1363
Bt22w 1505
Bt22c 1519
Bt19w 1361
Bt19c 1391
Bt23w 1507
Bt23c 1496

Software

Trimming of adaptor sequences and removal of reads with low quality: Trimmomatic
Alignment to the reference genome: Bowtie2
Filtering: SAMtools
Peak calling, generation of fold enrichment tracks: MACS2
Calling of nucleosome position and occupancy: DANPOS

Flow Cytometry

Plots

Confirm that:

☒ The axis labels state the marker and fluorochrome used (e.g. CD4-FITC).

☒ The axis scales are clearly visible. Include numbers along axes only for bottom left plot of group (a 'group' is an analysis of identical markers).

☒ All plots are contour plots with outliers or pseudocolor plots.

☒ A numerical value for number of cells or percentage (with statistics) is provided.

Methodology

Sample preparation

Cells were fixed in 75% of ethanol. After washing with 1xPBS twice, cells were suspended in Propidium iodide (PI) and RNase A, and incubated for 30 minutes at room temperature in the dark.

Instrument

Flow Cytometer and Cell Sorter workstation (BD FACSAriaIII)

Software	FlowJo
Cell population abundance	No flow sorting was applied.
Gating strategy	No gating strategy is applied for the yeast cells.

☐ Tick this box to confirm that a figure exemplifying the gating strategy is provided in the Supplementary Information.